

RESEARCH

Open Access



# Experimental and Numerical Assessment of Reinforced Concrete Beams with Disturbed Depth

A. Hamoda<sup>1</sup>, A. Basha<sup>1</sup>, S. Fayed<sup>1</sup> and K. Sennah<sup>2\*</sup>

## Abstract

This paper investigates numerically and experimentally the performance of reinforced concrete (RC) beam with unequal depths subjected to combined bending and shear. Such beams can geometrically be considered for unlevelled reinforced concrete (RC) floor slab-beam system. However, it may generate critical disturbances in stress flow at the re-entrant corner (i.e. location of drop in beam depth). This research investigates the use of shear reinforcement and geometric properties to enhance cracking characteristics, yielding, ultimate load-carrying capacity, and exhibiting ductile failure mode. Ten reinforced concrete (RC) beams were constructed and tested experimentally considering the following key parameters: recess length, depth of smaller beam nib, and amount and layout of shear reinforcement at re-entrant corner. Finite element analysis (FEA) with material non-linearity was conducted in two RC beams that were tested experimentally to validate the computer modelling. The FEA models were then extended to conduct a parametric study to investigate the influence of geometric parameters (beam shape and width) and amount and arrangement of shear reinforcement on the structural response. Results confirmed that geometric properties and ratio of shear reinforcement at the re-entrant region significantly affect the behavior of reinforced concrete beam with unequal depths in terms of first cracking, yielding level, ultimate load carrying capacity and mode of failure.

**Keywords:** beam with unequal depth, shear resistance, re-entrant corner, finite element simulation, concrete damage plasticity model, beam nib, ultimate load-carrying capacity

## 1 Introduction

Recently, reinforced concrete (RC) beams with constant depth are commonly employed in RC structures. Beams with unequal depth can geometrically be considered to accommodate unlevelled floor slab system and to allow for utilities (i.e. pipes and HVAC ducts) to go through the beam depth without increasing floor height. Figure 1a shows a schematic diagram of this beam of depth “t” and length “L” that has a reduced depth,  $h_n$ , over a length  $l_n$  (called recess length herein). The length of the beam with smaller depth is called “beam nib” and the region at which the beam depth changes from t to  $h_n$  is called “re-entrant corner” as depicted in Fig. 1a. The presence

of abrupt change in beam depth is expected to lead to (i) very critical flow of internal flexural stresses with its peak at the re-entrant corner (Nagy-György et al. 2012; Sas et al. 2014; Lim et al. 2016) and (ii) significant change in initial cracking, yielding level, ultimate load-carrying capacity and mode of failure (Kassem 2015; Zhong et al. 2017). Such critical transition zone can be called as disturbed region (D-region).

Another type of concrete beam with unequal depth is the one used in precast concrete beams and girders at their supports which is referred to as “dapped-end beams” (Hawileh et al. 2017). However, such beam configuration is outside the scope of the current research. Few researchers investigated the effect of span-to-depth ratio and shear span-to-depth ratio on the shear strength of concrete beams including the D-regions and dapped ends (Hu and Wu 2018; Choi et al. 2018; Qeshta et al.

\*Correspondence: ksennah@ryerson.ca

<sup>2</sup> Civil Engineering Department, Ryerson University, Toronto, ON, Canada

Full list of author information is available at the end of the article

Journal information: ISSN 1976-0485 / eISSN 2234-1315

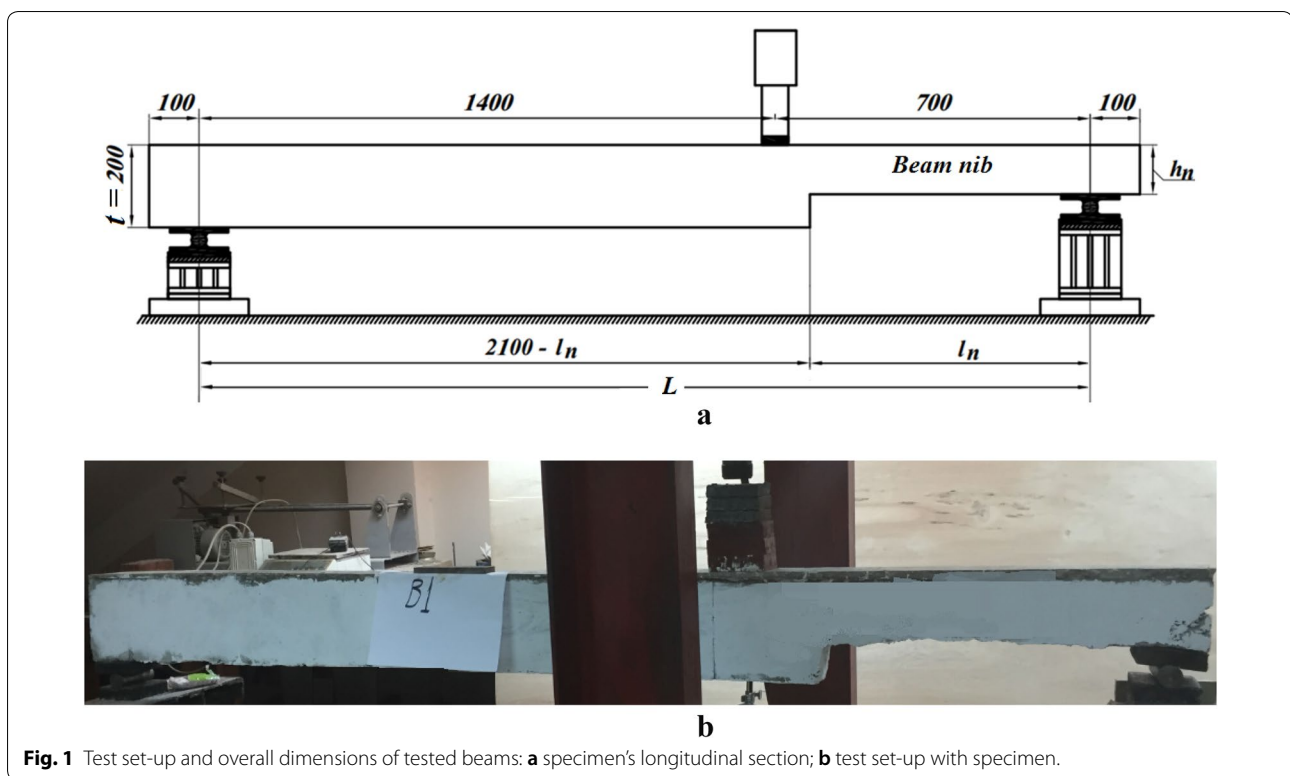


**Fig. 1** Test set-up and overall dimensions of tested beams: **a** specimen's longitudinal section; **b** test set-up with specimen.

2016; Naik and Kute 2013). Addition of shear reinforcement to intercept the D-region with excessive tensile stresses added to the ductile failure and ultimate load carrying capacity of the beam (Nagrodzka-Godycka and Piotrkowski 2012). Desnerck et al. (2016, 2017) investigated experimentally the impact of the reinforcement lay-out and amount as well as anchorage zone cracking on the load capacity of RC beams with dapped region, called “half-joint beams” in their research. They concluded that the arrangement of shear reinforcement in the form of vertical steel bars, U-shape bars and diagonal bars at the dapped end affect the initiation of concrete cracking, yielding of reinforcement and load capacity at this disturbed beam end. Zhong et al. (2017) proposed an evaluation system to assess conveniently the performance of D-regions designed using different strut-and-tie models. Results showed that reinforcement lay-out, respect to strut-and-tie models, can significantly affect mode of failure and ultimate capacity. Aswin et al. (2015) examined experimentally the behavior of dapped-end beam failed by excessive shear stresses at the nib area. Using ductile engineered cementitious composite (ECC) at dapped-end zone would lead to enhanced shear strength and ductility as demonstrated for composite girder investigated elsewhere (Hamoda et al. 2017; Hossain et al. 2015). Fang et al. (2018) studied experimentally horizontal shear behavior of normal and lightweight concrete composite

T-beam. Fernández et al. (2018) studied experimentally the performance of beams having D-region designed using fundamentals of strut-and-tie model. Others (Desnerck et al. 2018; Pradhan et al. 2018; Alam et al. 2017; El Bitouri et al. 2017; Nosheen et al. 2018; Demir et al. 2016; Chiu et al. 2016; Kobiellak and Zamiar 2017) investigated experimentally and numerically the shear behavior of reinforced concrete members with various types of reinforcement lay-out.

Literature review revealed that the structural behavior of reinforced concrete beam with reduced beam depth over a significant portion of the beam span, as depicted in Fig. 1a, is as yet unavailable. Such change in beam depth within the beam span would cause significant flexural stiffness loss and would lead to premature brittle failure at the re-entrant corner due to stress concentration and change in beam flexural and shear stiffness. As such, the objective of this research is to investigate the structural response of such beam configuration under increasing static loading to collapse as affected by (i) the ratio between beam depths ( $h_n/t$ ), (ii) recess length/beam span ratio ( $l_n/L$ ), (amount and arrangement of shear reinforcement and the re-entrant region, and (vi) change in beam width at the disturbed region. Ten RC beams were constructed and then tested under increasing static loading up to failure. A nonlinear three-dimensional finite element analysis (FEA), utilizing an available concrete

damage plasticity (CDP) model, was performed in two of the tested beams to expand on the study of key parameters affecting the structural response of beams with abrupt change in its depth within its span. The experimental test results and the numerical modelling are presented for discussion herein in the form of cracking and yielding characteristics, load-carrying capacity and failure mode. Then, conclusions are drawn regarding improving crack appearance, ductility, and load-carrying capacity of the studied beams. The outcome of this research will allow designers to better understand the structural performance of such structural elements for practical construction applications, particularly in buildings.

## 2 Experimental Study

The experimental testing program included the construction of 10 simply-supported reinforced concrete beams, followed by testing them under static loading to failure. The tested beams were divided into 5 groups with respect to the length of the beam nib,  $l_n$ , depth of the beam nib,  $h_n$ , and amount and layout of shear reinforcement at the re-entrant corner. In all these beams, the beam width,  $b$ , was taken as 100 mm, the overall depth,  $t$ , was taken as 200 mm and the beam span,  $L$ , was taken as 2100 mm. All beams were subjected to a concentrated load which was applied at  $0.33 L$  to ensure that the re-entrant corner and the beam nib are subjected to high shear stresses, leading to failure on that side of the beam. Figure 1a shows beam

dimensions and a schematic diagram of the three-point loading arrangement, while Fig. 1b shows a photo of the beam setup before testing. The following subsections summarize the description of beam groups, materials properties, test setup and test procedure. Table 1 summarizes the details of the tested beam groups.

### 2.1 Description of Tested Beam Groups

Figure 2 summarizes the reinforcement details for each of the 10 beams considered in this study. To study few geometric parameters and effect of shear reinforcement on the ultimate capacity and failure modes, the tested beams have similar flexural reinforcement in the form of 2#10 bars in the tension side of the beam and 4#10 bars in the compression side of the beams as depicted in Fig. 2 to ensure tension-control failure based on the size of the beam and the availability of minimum steel bar sizes to conduct such small scale testing. The development length of the tension bars in the beam nib projecting into the beam portion with deeper section was taken 150 mm for all beams as depicted in Fig. 2d.

Beam group (1) consisted of two beams, namely: B0 and B2. Beam B0 was constructed with constant depth of 200 mm, while beam B2 had a nib with depth,  $h_n$ , of 120 mm (i.e.  $h_n/t=0.6$ ) and recess length,  $l_n$ , of 600 mm (i.e.  $l_n/L=0.3$ ). Figure 2a, b) show dimensions and reinforcement details for beams B0 and B2, respectively. Such group aims at assessing the major difference of ultimate load-carrying capacity and failure mode observed from

**Table 1** Details of tested beams.

Specimen	Group	$f_c$ (MPa)	$l_n$ (mm)	$l_n/L$	$h_n$ (mm)	$h_n/l_n$	$h_n/t$	Shear reinforcement ratio	
								$V_{sd}$ %	$V_{sb}$ %
B0	G1	31.54	–	1.00	–	–	–	–	–
B2		29.82	630	0.30	120	0.19	0.60	0.50	0.50
B2	G2	29.82	630	0.30	120	0.19	0.60	0.50	0.50
B1		33.36	525	0.25	120	0.23	0.60	0.50	0.50
B3		32.18	315	0.15	120	0.38	0.60	0.50	0.50
B4	G3	31.72	525	0.25	80	0.15	0.40	0.50	0.50
B1		33.36	525	0.25	120	0.23	0.60	0.50	0.50
B5		32.26	525	0.25	160	0.30	0.80	0.50	0.50
B1	G4	33.36	525	0.25	120	0.23	0.60	0.50	0.50
B6		32.02	525	0.25	120	0.23	0.60	0.50	0.80
B7		30.67	525	0.25	120	0.23	0.60	0.80	0.50
B1	G5	33.36	525	0.25	120	0.23	0.60	0.50	0.50
B8		31.59	525	0.25	120	0.23	0.60	0.80	0.80
B9		32.48	525	0.25	120	0.23	0.60	0.53*	0.53*

$l_n$ , length of beam nib;  $h_n$ , height of beam nib;  $t$ , beam height;  $V_{sd}$  %, ratio of shear reinforcement in volume for nib zone;  $V_{sb}$  %, ratio of shear reinforcement in volume for beam portion with greater depth. \* $V_{sd}$  % for stirrups plus 2 local bent bars at the re-entrant corner (see Fig. 2j).

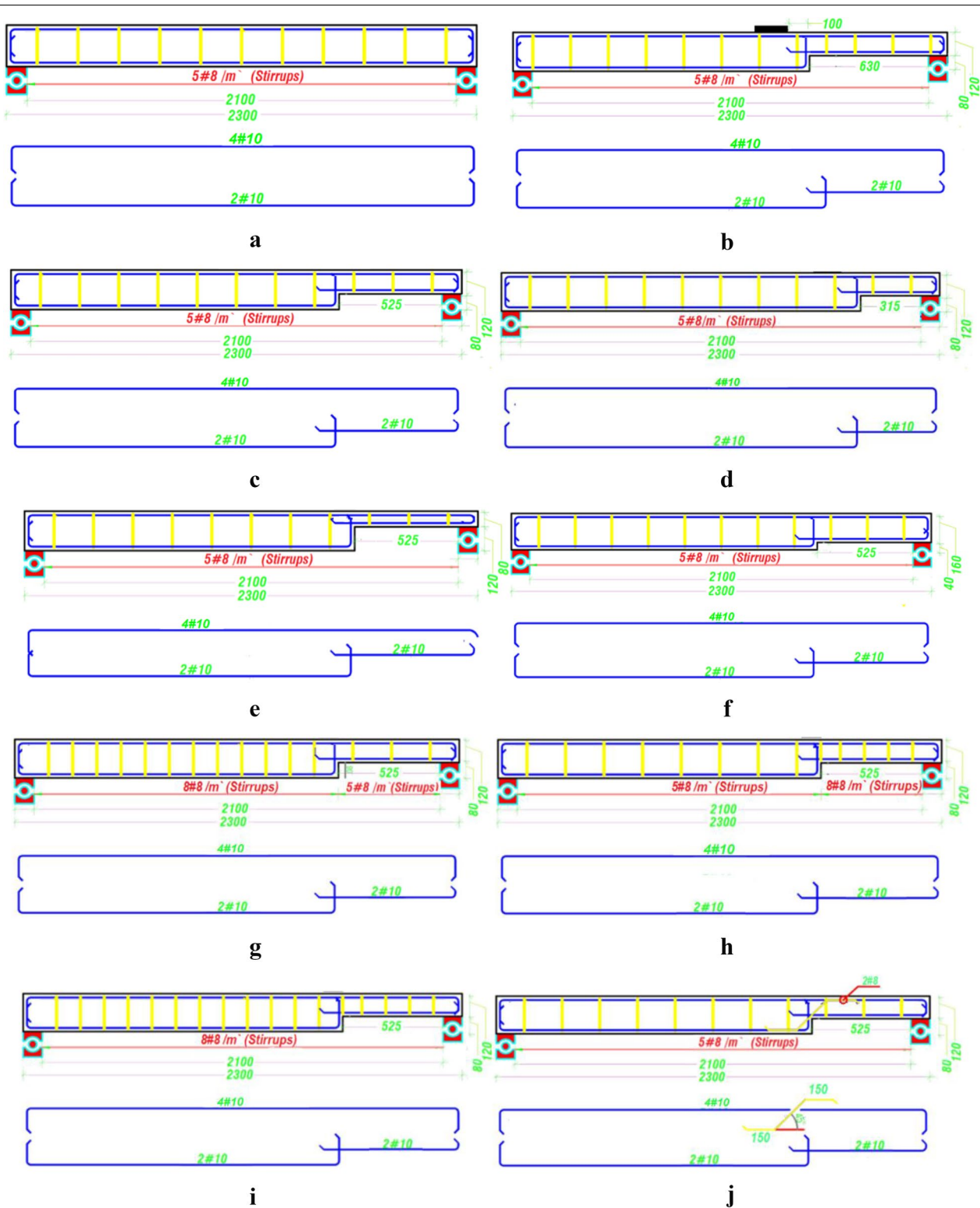


**Fig. 2** Geometric details of steel arrangement for all tested beams: **a** Beam B0 (G1); **b** Beam B2 (G1); **c** Beam B1 (G2); **d** Beam B3 (G2); **e** Beam B4 (G3); **f** Beam B5 (G3); **g** Beam B6 (G4); **h** Beam B7 (G4); **i** Beam B8 (G5); **j** Beam B9 (G5) (notes: for all beams, the embedment length for bottom reinforcement extended from beam nib equaled to 200 mm).

the conventional beam B0 and beam B2 with re-entrant corner.

Beam group (2) consisted of three beams, namely: B1, B2 and B3. Beams B1 and B3 were identical to beam B2 with respect to geometry and reinforcement except that the recess lengths,  $l_n$ , were 630, 525, and 315 mm, respectively, leading to  $l_n/L$  ratios of 0.30, 0.25 and 0.15. Figure 2c, d show dimensions and reinforcement details of beams B1 and B3, respectively. This group was intended to examine the effect of the recess length with reduced depth on the structural behavior of the beam.

Beam group (3) had 3 beams, namely: B1, B4 and B5. Beams B4 and B5 were identical to beam B1 with respect to dimensioning and reinforcement, especially the recess length,  $l_n$ , of 525 mm. However, their nib depth,  $h_n$ , were taken 80, 120 and 160 mm for beams B4, B1 and B5, respectively, leading to  $h_n/l_n$  ratios of 0.15, 0.23 and 0.3. Figure 2e, f show dimensions and reinforcement details for beams B4 and B5, respectively. The main objective of this beam group was to evaluate the effect of nib depth on the beam ultimate capacity and failure mode.

Beam group (4) consisted of 3 beams, namely; B1, B6 and B7. These beams were identical with respect to beam geometry and arrangement and amount of flexural reinforcement. However, the amount of shear reinforcement in each of these beams was different. The amount of stirrups to resist shear force in the beam portion with depth,  $t$ , of 200 mm, was taken as 5#8/m, 8#8/m and 5#8/m for beams B1, B6 and B7, respectively, leading to shear reinforcement ratio,  $V_{sb}\%$ , as 0.50, 0.80 and 0.50, respectively. On the other hand, the amount of stirrups to resist shear force in the beam nib with depth,  $h_n$ , of 120 mm, was taken as 5#8/m, 5#8/m and 8#8/m for beams B1, B6 and B7, respectively, leading to shear reinforcement ratio in the beam nib,  $V_{sd}\%$ , as 0.50, 0.50 and 0.80, respectively. Figure 2g, h show dimensions and reinforcement details for beams B6 and B7, respectively. The main objective of this beam group was to evaluate the effect of the amount of stirrups in the beam full depth or in the beam nib on the beam ultimate capacity and failure mode.

Beam group (5) consisted of 3 beams, namely; B1, B8 and B9. These beams were identical with respect to beam geometry and arrangement and amount of flexural reinforcement. However, the amount of shear reinforcement in each of these beams was different. The amount of stirrups to resist shear force in beam B1 was taken 5#8/m, leading to shear reinforcement ratio,  $V_{sb}\%$ , or  $V_{sd}\%$  of 0.50. On the other hand, the amount of stirrups to resist shear force in beam B8 increased to 8#8/m as depicted in Fig. 2i, leading to shear reinforcement ratio,  $V_{sb}\%$  or  $V_{sd}\%$  of 0.80. To address the effect of local strengthening of the re-entrant corner in shear, 2#8 bent-up bars were added at 45° angle at the interface between the beam nib

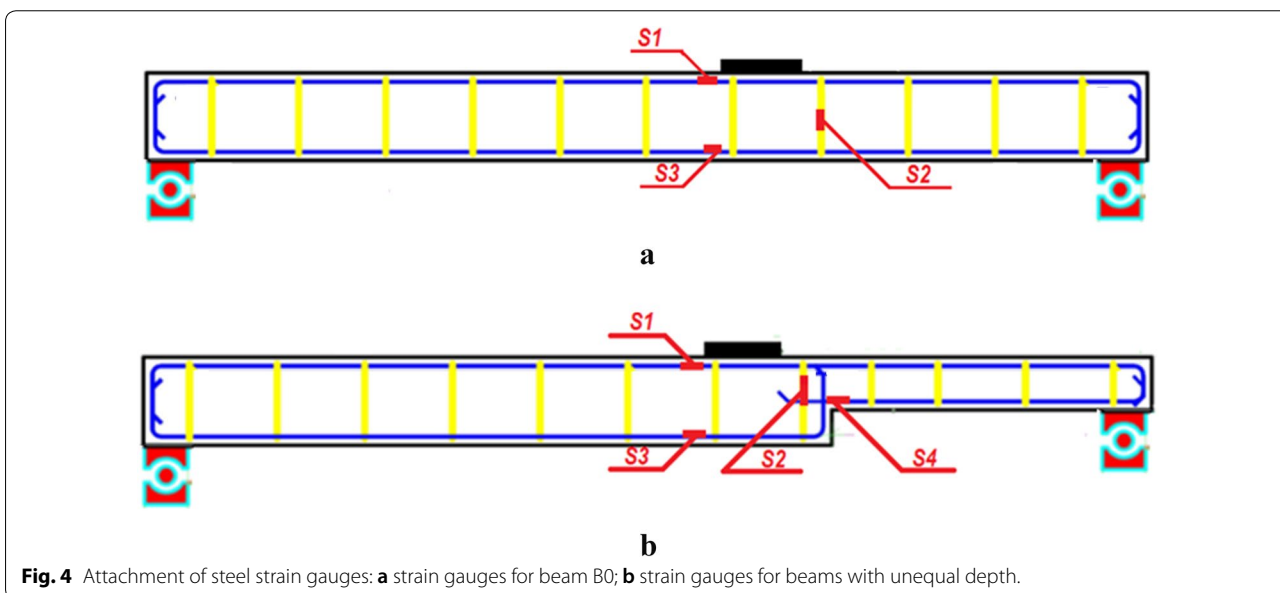
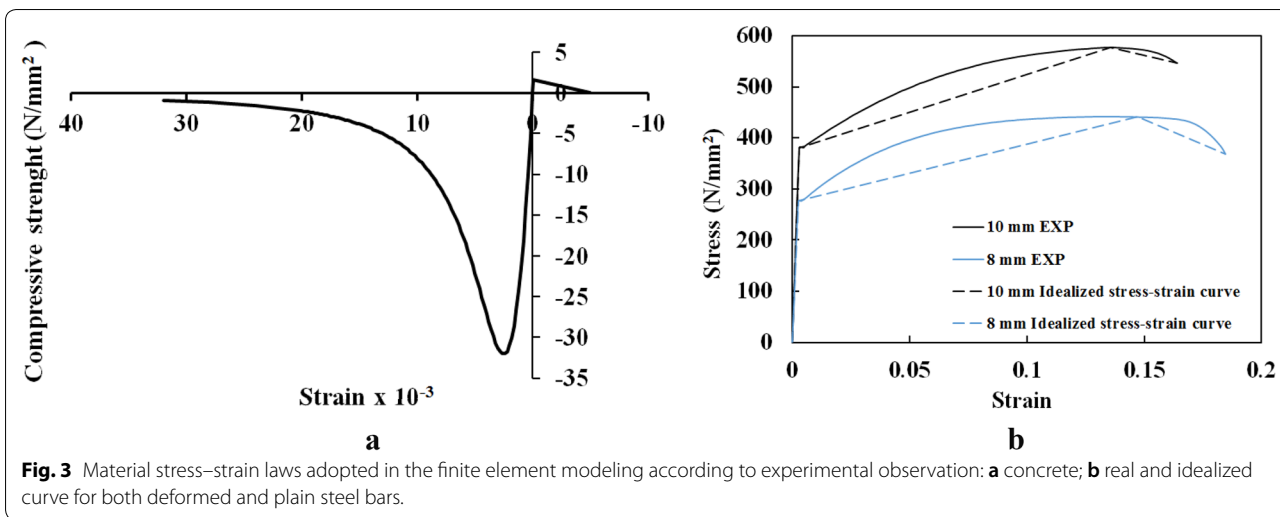
and the beam portion with deeper section as depicted in Fig. 2j. This leads to an average shear reinforcement ratio ( $V_{sb}\%$  or  $V_{sd}\%$ ) of 0.52. The main objective of this beam group was to evaluate the effect of the amount of shear reinforcement when it is kept constant all over the span of the beam.

## 2.2 Material Properties

Normal strength concrete was employed for casting. Such concrete consisted of Ordinary Portland Cement, natural siliceous sand, crushed pink hard limestone with 10 mm maximum nominal size and water, with mix proportions by weight as 1: 2: 3.18. The concrete mix had water cement ratio of 0.53. The average value of concrete compressive strength was about 32.0 MPa, however, average concrete compressive strength for each beam is listed in Table 1. Two types of reinforcing steel bars were used in this study. Deformed steel bars with 10 mm diameter conforming with Grade 369/534 steel was used as tension and compressive reinforcement for flexural resistance. Plain bars of 8 mm diameter conforming with Grade 293/467 steel was used for vertical stirrups and bent-up bars as shear reinforcement. Idealized stress–strain curves for concrete in compression and tension used in the finite element analysis (FEA) modelling are shown in Fig. 3a. Steel material stress–strain curves obtained from testing steel coupon tensile testing as well as idealized stress–strain curves adopted for FEA modeling are shown in Fig. 3b.

## 2.3 Test Setup and Test Procedure

After 28 days from casting, each beam was placed, centered and leveled at the support zone as shown in Fig. 1b. All beams rest over hinged support on one side, allowing for rotation with no displacement, while the other support allows for horizontal movement and rotation, simulating roller support. A concentrated load was applied at 0.33 L as depicted in Fig. 1a in order to generate high shear force at the re-entrant corner. It should be noted that the distance between the edge of the steel base plate, transferring the applied load to the beam, to the re-entrant corner was taken as 100 mm as depicted in Fig. 2b for all tested beams. Electrical strain gauges were installed in selected steel bars as depicted in Fig. 4. Three strain gauges were attached at the solid beam. B0 as depicted in Fig. 4a, while four gauges were mounted on beams with unequal depths as shown in Fig. 4b. One dial gauge of 0.01 mm accuracy was used to record beam vertical deflection at load location as shown in Fig. 1b. The load was applied in 0.2 kN increments up to failure. During each load increment, cracks (if any) were marked and deflection and steel strain readings were recorded. The duration of each increment was about 2 min. Failure



was considered attained when the beam could not take further load.

**2.4 Test Results and Discussion**

Figures 5, 6, 7, 8 and 9 shows photos of the crack pattern after failure of each beam. Table 2 provides the experimental findings in the form of cracking load ( $P_{cr}$ ), and corresponding beam deflection ( $\Delta_{cr}$ ), zone at which first crack appeared, yield load ( $P_y$ ) and first location of bar yield, ultimate load ( $P_u$ ) and corresponding deflection at failure ( $\Delta_u$ ) and failure mode for each tested beam. The following subsection discuss the experimental findings in details.

**2.4.1 Crack Pattern and Failure Mode**

**2.4.1.1 First Group (G1)** For the first group, the first visible hair crack for the control beam B0 (with no nib zone) was flexural-shear appearing at the bottom surface of section at applied load location at about 15.20 kN (34% of ultimate load). As the applied load increased, several flexural and flexural-shear cracks appeared close to the bottom surface of the beam and gradually extended towards its top surface. However, a major diagonal crack appeared at beam mid-depth at a load of 38 kN (86% of ultimate load). Such crack continued to enlarge at higher loads and propagated towards the top surface close to edge of the loading plate and downward towards the bottom surface close to the supporting plate. Then, sudden concrete



**Fig. 5** Crack patterns of group G1: **a** side and top surfaces of Beam B0; **b** side, top surfaces of beam B2; **c** re-entrant corner of beam B2.

crushing occurred at the top surface close to loading plate, as shown in Fig. 5a, causing beam failure at an ultimate load of 44.40 kN in a shear-compression failure mode.

Beam B2 shown Fig. 5b in first group (G1) had the first visible flexural crack at an applied load of about 3.00 kN (19% of ultimate load) initiating from the re-entrant corner of the nib zone, as expected. Then, a few cracks grew from the first initial one at a load ranging from about 26% to 58% of the ultimate load. As the applied load increased, a few flexural and shear-flexural cracks appeared. These cracks continued to enlarge and propagate from the bottom of the beam towards the top surface of the beam. Just before failure, the flexural major crack formed at re-entrant corner propagated towards the compressive side of the beam and spread laterally giving the signs of approaching concrete crushing at the top surface of the beam as depicted in Fig. 5b. The beam could not take an applied load beyond 15.10 kN presenting a pure flexural failure mode at the re-entrant corner of the nib region.

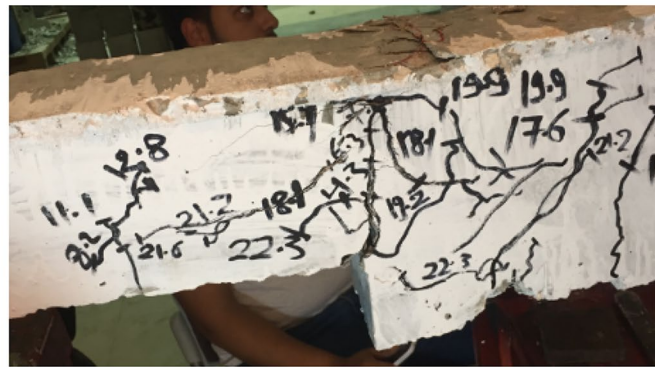
**2.4.1.2 Second Group (G2)** The second group (G2) was considered to study the effect of recess length,  $l_n$ , of 630 mm, 525 mm and 315 mm, for beams B2, B1, and B3,

respectively (i.e.  $l_n/L=0.3, 0.25$  and  $0.15$ , respectively). Beam B1 with a nib length-to-beam length ( $l_n/L$ ) of 0.25 exhibited the first visible hair crack at the re-entrant corner at an applied load of about 3.00 kN (19% of ultimate load). As the load increased, several cracks appeared in the re-entrant zone as shown in Fig. 6a. In addition, very few flexural cracks appeared at the bottom surface at section close to loading plate and propagated towards the top of the beam with increase in applied loading. Just before failure, the major crack formed at the re-entrant corner became wider propagating upward toward the top surface at an angle leading to shear-compression failure mode at a load of 15.70 kN with signs of concrete crushing at the top fibers.

Figure 6b shows crack pattern for beam B3 with  $l_n/L$  of 0.15. As expected, the first visible crack appeared at the re-entrant-corner of nib zone at an applied load of about 4.30 kN (17% of the ultimate load). As the load increased, several cracks appeared before and after the re-entrant corner. These cracks propagated at an angle towards the top surface as well as the direction of the loading plate, leading to sudden concrete crushing in concrete at the top surface of the beam beside the steel loading plate as



a



b

**Fig. 6** Crack patterns of group G2: **a** side and top surfaces of Beam B1; **b** top surfaces and re-entrant corner of beam B3.

shown in Fig. 6b. with an ultimate load,  $P_u$  of 24.80 kN. The beam could not sustain an applied load beyond 24.8 kN due to shear-compression failure.

By comparing the results of the three beams in this group, one may observe the change in the failure mode from flexural in a beam with longer beam nib (beam B2) to shear-compression failure in a beam with shorter beam nib (beams B1 and B3). Also, it can be observed that the beam load carrying capacity increases with decrease in beam nib length. For example, the beam capacity increased by 64% with decrease of nib length from 630 mm to 315 mm. On the other hand, slight increase in beam capacity (i.e. 2%) when reducing the nib length from 630 to 525 mm. Similar behavior was observed in case of observed cracking load of beams B2, B1 and B3.

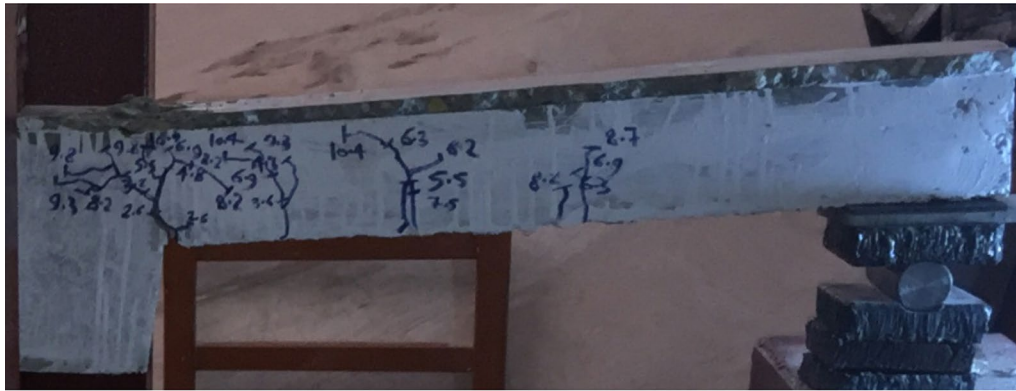
**2.4.1.3 Third Group (G3)** The third group (G3) was considered to investigate the change in the depth of the beam nib to the main beam depth on the structural response. In

this case, Beams B4, B1 and B5 had the same nib length of 525 mm while the nib depth,  $h_n$ , was taken as 80, 120 and 160 mm, respectively.

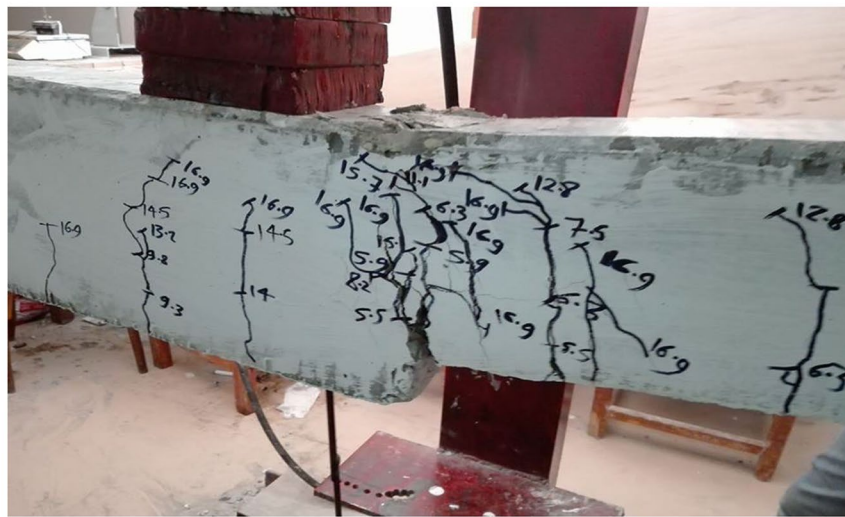
For beam B4 with  $h_n$  of 80 mm, the first visible crack appeared at the re-entrant corner at a load of about 2.60 kN (25% of the ultimate load). As the load increased, several flexural-shear cracks appeared in the beam nib region and propagated towards the top surface of the beam. A sudden concrete crushing occurred at the top surface of the beam between the edge of loading plate and the re-entrant corner causing shear-compression failure at a load of 10.40 kN as depicted in Fig. 7a.

For beam B5 with  $h_n$  of 160 mm, the first visible crack occurred at the re-entrant corner at a load of 5.50 kN (31% of ultimate load). The first flexural crack appeared at bottom surface close to the loading location at a load of 9.30 kN (53% of ultimate load). With increase in the applied load, several flexural-shear cracks appeared in the nib zone and propagated towards the steel loading





a



b

**Fig. 7** Crack patterns of group G3: **a** side surface of Beam B4; **b** top surfaces and re-entrant corner of beam B5.

plate direction, leading to sudden concrete crushing at the top surface of the beam between the loading plate and the re-entrant corner as shown in Fig. 7b. The beam failed in a shear-compression failure mode at an ultimate load of 21 kN.

By comparing the results of the three beams in this group, one may observe that the increase in the depth of the beam nib compared to the main depth of the beam did not alter the failure mode which was shear-compression failure. However, the beam load carrying capacity increased with increase in beam nib depth, as expected. For example, the beam capacity increased by 51% and 102% with increase of nib depth from 80 mm to 120 mm and 160 mm, respectively. Also, the beam first cracking load increased by 15% and 211% with increase of nib depth from 80 mm to 120 and 160 mm, respectively, as expected.

**2.4.1.4 Fourth Group (G4)** The main purpose of the fourth group G4 was to examine the effect of the amount of stirrups in the beam nib and the beam portion with the main depth of 200 mm on the structural response. In this case, 3 beams (B1, B6 and B7) of equal nib length and depth of 525 mm and 120 mm, respectively, were considered but with different stirrup spacing in each of the beam nib and the main beam portion. Beam B6 was reinforced with rectangular closed stirrups with diameter of 8 mm placed at 200 mm spacing in the main beam portion, while the nib region had the same stirrups at 125 mm spacing. Figure 8a shows the crack pattern of beam B6 after failure. The first crack appeared at the re-entrant corner with a load of 3.60 kN (23% of the ultimate load). Also, the first flexural crack was recorded at the bottom surface of loading location at a load of 8.20 kN (53% of ultimate load). As the load increased, several hair cracks were generated and propagated to the top surface of the beam in the region between



**Table 2 Test results.**

Designation	Group	Cracking properties			$P_y$ (kN)	Location of first yield	$P_u$ (kN)	$\Delta_u$ (mm)	Mode of failure
		$P_{cr}$ (kN)	$\Delta_{cr}$ (mm)	Region					
B0	G1	15.20	2.35	MS	33.8	F	44.40	9.91	SC
B2		3.00	0.45	RE	11.49	H	15.10	15.65	F
B2	G2	3.00	0.45	RE	11.49	H	15.10	15.65	F
B1		3.00	0.49	RE	14.62	H	15.70	19.50	SC
B3		4.30	0.48	RE	22.30	H	24.80	15.13	SC
B4	G3	2.60	0.30	RE	8.48	H	10.40	18.00	SC
B1		3.00	0.49	RE	14.62	H	15.70	19.50	SC
B5		5.50	0.91	RE	18.38	H	21.00	28.59	SC
B1	G4	3.00	0.49	RE	14.62	H	15.70	19.50	SC
B6		3.60	0.89	RE	17.75	H	20.50	18.99	SC
B7		3.20	0.24	RE	16.72	H	19.00	13.60	SC
B1	G5	3.00	0.49	RE	14.62	H	15.70	19.50	SC
B8		4.30	0.43	RE	19.78	H	21.00	17.85	F
B9		5.90	1.56	RE	16.65	B	21.00	18.96	SC

$P_{cr}$ , load at which first crack occurred;  $\Delta_{cr}$ , deflection recorded at first crack;  $P_y$ , load at which first yield occurred;  $P_u$ , ultimate load;  $\Delta_u$ , deflection recorded at ultimate load; F, first yield load recorded at flexural bar; H, first yield load recorded at horizontal bar; B, first yield load recorded at bent-up bar; MS, mid-length of strut connect between edge of loading plate and support; RE, re-entrant corner; S, shear failure; SC, shear-compression failure; F, flexural failure.

the re-entrant corner and the loading plate. However, no cracks were detected at the nib region as shown in Fig. 8a. The main diagonal shear crack at the re-entrant corner propagated to the edge of the loading plate causing slight concrete crushing at an ultimate load of 20.5 kN in a form of shear-compression failure mode.

Beam B7 had stirrup arrangement opposite to that for beam B6. Beam B7 was reinforced with rectangular closed stirrups with diameter of 8 mm placed at 125 mm spacing in the main beam. As shown in Fig. 8b, the first visible crack appeared diagonally at the re-entrant corner at a load of 3.20 kN (24% of the ultimate load). In contrast to beam B6, flexural and flexural-shear cracks appeared in both sides of the re-entrant corner of Beam B7. Failure of Beam B7 occurred due to sudden concrete crushing at the top surface of the beam beside the loading plate. Perfect shear-compression failure mode was observed at an ultimate load of 19 kN. Comparison between beams B1 and B6 in this group showed that the increase in stirrup amount in the nib region has significant effect in the load carrying capacity (i.e. 31% difference), with the cracking load increased by 20%. Comparison between beams B6 and B7 in this group showed that the increase in stirrup amount in the main beam segment rather than the nib region decreased the load carrying capacity and the cracking load by 8% and 13%, respectively.

**2.4.1.5 Fifth Group (G5)** The last group aimed at studying the effect of shear reinforcement amount when it is

maintained the same all over the beam span. Figure 9a shows cracking pattern of the tested beam B8 with stirrup spacing of 125 mm. The first visible crack appeared at the re-entrant corner at a load of 4.30 kN (25% of the ultimate load). The first flexural crack remarked at the bottom surface of nib region as well as loading location at a load of 5.50 and 8.20 kN (32% and 48% of the ultimate load) respectively. As the load increased, several flexural cracks appeared and propagated towards the top surface of the beam. the flexural crack at the re-entrant corner propagated vertically towards the top surface of the beam, followed by sudden concrete crushing as shown in Fig. 9a. Flexural failure mode was observed at an ultimate load of 21 kN.

Beam B9 was identical to beam B1 with respect to stirrup spacing of 200 mm all over the length of them beam except that 2#8 bent-up bars were added at 45° angle at the re-entrant corner as depicted in Fig. 2j. In beam B9, the first crack was observed at a load of 5.90 kN (34% of the ultimate load) initiating from re-entrant corner. As the applied load increased, other flexural and flexural-shear cracks appeared and propagated towards the top surface of the beam. However, major diagonal shear crack at the re-entrant corner zone propagated to the top surface of beam causing sudden concrete crushing, as depicted in Fig. 9b, at an ultimate load of 21.00 kN. The comparison between beams B9 and B8 showed that the number of flexural cracks in beam B8 were almost greater than those observed from other counterparts which may

attributed to the presence of augmented closed stirrups along the entire beam span including the nib region. In addition, the failure mode was mainly flexural in contrast to the shear-compression failure modes in other beams in this group. Also, one may observe that the increase in stirrup amount increased the ultimate load and the cracking load by 33% and 43%, respectively, when comparing beams B1 and B8.

When comparing beams B1 and B9, it can be observed that the addition of the 2#8 bent-up bars at the re-entrant corner increased the cracking load and the ultimate load by 97% and 34%. In conclusion, the increase of shear reinforcement delayed the start of flexural cracks and increased the ultimate load capacity in the studied beams.

### 2.5 Load–Deflection Response

Figure 10 summarizes the load–deflection relationship for the tested beams in each group. It should be noted that beam deflection was recorded at the location of the applied load. Table 2 provides the deflection values at cracking load ( $\Delta_{cr}$ ) and ultimate load ( $\Delta_u$ ).

As it can be seen in Fig. 10, the all tested groups showed a linear response before the cracking load which was recorded to be between 3.0 and 5.9 kN for the beams with nibs and 15.2 kN for the beam with constant depth. Then, the load–deflection responses were almost linear to the yield load level, and became almost nonlinear afterwards. As expected, the recess length (nib length) appeared to have a significant influence on the deflection values all over the loading history.

For beam group G2, Fig. 10b shows similar deflection response for beams with recess lengths of 630 and 525 mm, with very much less deflection in the beams with 315 mm recess length at the same load level, as expected. Given the increase in ultimate load capacity in beam B3, its ultimate deflection was recorded as 23.75 mm compared to 15.65 and 15.14 mm for beams B2 and B1, respectively.

Figure 10c shows the load–deflection relationship for beam group G3 at which the nib height was the main variable. At the cracking load level, one may observe the increase in cracking load deflection with increase in nib depth. Similar behavior was observed for the ultimate deflection at failure. As depicted in Table 2, it can be observed that although the failure mode of all beams in this group is compression-shear failure, the ultimate deflection increases with the increase in nib depth.

Load–deflection relationship for beam group G4 is shown in Fig. 10d. Since the load–deflection curves overlapped with each other, one may conclude that the change in the amount of shear reinforcement in each of the main beam portion or the beam nib does not

have an insignificant effect on the deflection values at a given load. Similar conclusion is observed in Fig. 10e with the change in the amount of stirrup spacing all over the beam span or with the addition of the bent-up bars at the re-entrant corner for beam group G5.

### 2.6 Steel Stress–Strain Relationship

Figures 11, 12, 13 and 14 show the load–steel strain relationship recorded during testing. For each group, load–steel strain were depicted from four gauges mounted on compressive bar, vertical stirrup, flexural bar and horizontal bar (gauges S1, S2, S3 and S4, respectively, in Fig. 4b). Table 2 shows the load value at which the yield strain first reached and the corresponding location in these bars. Based on the tensile testing of the bar specimens, the yield strain considered in this study is 0.00185 (359 MPa yield stress/200,000 MPa modulus of elasticity = 0.00185 yield strain).

Figure 11 shows the load–steel strain relationships at recorded locations in the horizontal bar in the beam nib, vertical stirrup close to the re-entrant corner, the flexural bar compression bars just at the load location. It can be observed that out of all these bars, yield strain reached in the horizontal bar in the tension side of the nib at the re-entrant location, as expected. The yield loads were at 76%, 93% and 90% of the ultimate load for beams B2, B1 and B3, respectively. This confirms the type of failure exhibited in each of these beams. Results show the ductile flexural failure in beams B2 of 630 mm nib length and the brittle shear-compression failure in case of beam B1 and B3 with nib lengths of 525 and 315 mm, respectively. This means that the shorter the nib length, the more brittle the failure mode.

Group G3 has similar behavior as group G2 as the yield strain reached first in the horizontal bar in the nib tension side at the re-entrant corner. The yield loads were at 82%, 93% and 88% of the ultimate load for beams B6, B1 and B7, respectively. Such change in yield load values does not provide a trend with the increase in nib height from 80 mm to 120 and 160 mm for this group as the failure mode of all beams were identical as shear-compression failure.

Group G4 exhibited the yield strain reaching first in the horizontal bar in the nib tension side at the re-entrant corner. The yield loads were at 93%, 87% and 88% of the ultimate load for beams B1, B6 and B7, respectively. Group G5 exhibited the yield strain reaching first in the horizontal bar in the nib tension side at the re-entrant corner. The yield loads were at 93%, 94% and 79% of the ultimate load for beams B1, B8 and B9, respectively. From results of groups G4 and G5, one may conclude that such change in yield load values does not provide a trend with

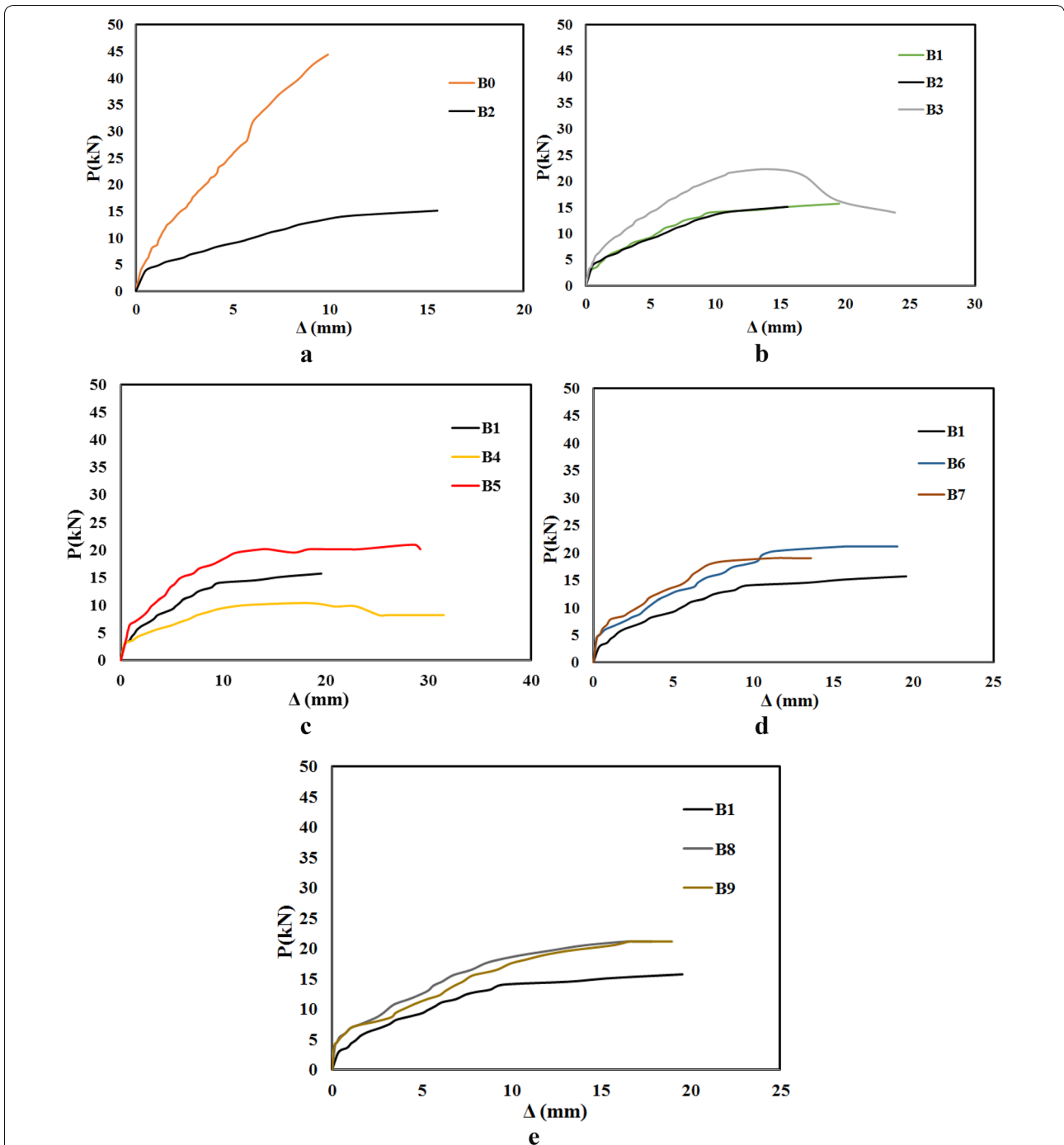


**Fig. 10** Load–deflection relationships for the tested specimens: **a** first group G1; **b** second group G2; **c** third group G3; **d** fourth group G4; **e** Fifth group G5.

the increase in amount of stirrups in the beam. However, the addition of the bent bar at the re-entrant corner rather than increasing the stirrup amount provided greater ductile behavior given the lower yield load level compared to other beams in the same group.

### 3 Numerical Simulations

This section provides detailed investigations on a developed nonlinear three-dimensional finite-element analysis (FEA) simulation, using ABAQUS software (ABAQUS/CAE 2014), for modeling simply-supported RC beam

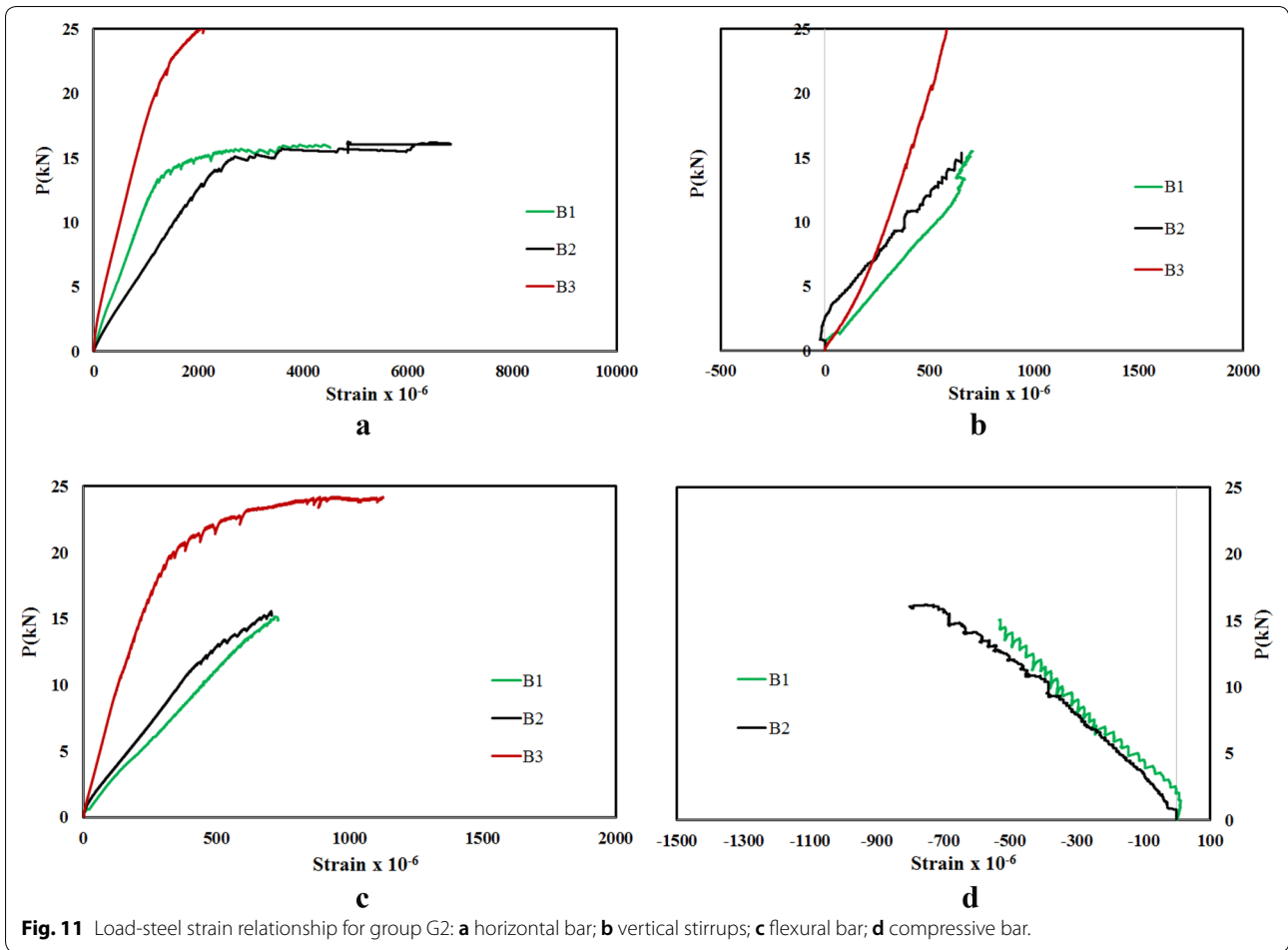


**Fig. 11** Load-steel strain relationship for group G2: **a** horizontal bar; **b** vertical stirrups; **c** flexural bar; **d** compressive bar.

with and without unequal depths, identical to that tested experimentally. The FEA model was validated using the experimental findings in terms of load-carrying capacity, crack pattern, failure mode, load-deflection response, load-steel strain relationship. Then, the model was used to conduct a parametric study and used for further researches.

### 3.1 Material Properties of Concrete and Steel in the FE Modeling

Concrete damage plasticity (CDP), smeared cracked and brittle cracking modelling defined in ABAQUS/Standard (ABAQUS/CAE 2014) were utilized to define concrete material properties. However, CDP model was used to constitute the plastic mechanical behavior of concrete herein over brittle or smeared cracked counterparts, since it utilizes the concept of isotropic damage elasticity in combination with isotropic compression and tension plasticity to simulate the nonlinear behavior of concrete under tensile and compressive stresses. The concrete

stress-strain response employed for modeling was calibrated respected to concrete compressive strength and splitting test tested experimentally. The stress-strain behavior used in the constitutive model for compression incorporates a formula developed by Carreira and Chu (Carreira and Chu 1985) as shown in Fig. 3a. The uniaxial tensile stress-strain exhibition was selected as a linear elastic response prior to collapse stress value obtained experimentally, beyond which, the stress was decreased linearly to zero value at which strain was about 0.005.

Based on the literature, the Yield Criteria (YC) developed by Lubliner et al. (1989), followed by some modifications by Lee and Fenves (1998), shown in Eq. (1) was employed for concrete:

$$YC = \frac{1}{1 - \alpha} \left[ \sqrt{3I_2} + \alpha I_1 + \beta * \varepsilon^{pl} \bar{S}_{max} - \gamma - \bar{S}_{max} \right] - \bar{S}_{max} * \varepsilon_c^{pl} \tag{1}$$

where  $\sqrt{3I_2}$  is the classical deviatoric stress measure,  $I_1$  refers to the hydrostatic pressure, ( $\bar{S}_{max}$ ) is the

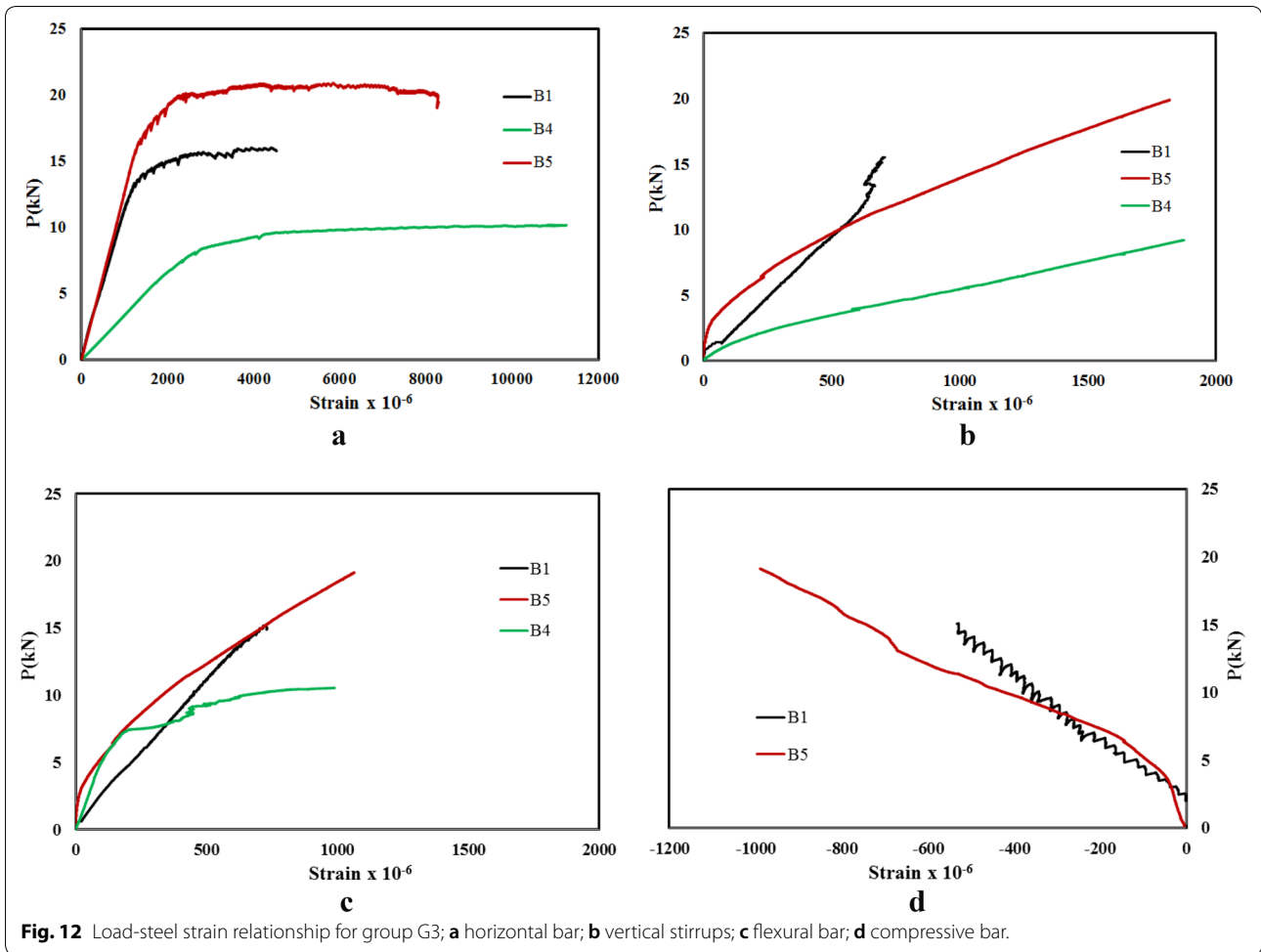


**Fig. 12** Load-steel strain relationship for group G3; **a** horizontal bar; **b** vertical stirrups; **c** flexural bar; **d** compressive bar.

algebraically maximum principal stress, the dimensionless values  $\alpha$ ,  $\beta$  and  $\gamma$  are can be evaluated as follows:

$$\alpha = \frac{s_{bo}/s_{co} - 1}{2(s_{bo}/s_{co}) - 1} \tag{2}$$

The ratio of biaxial-to-uniaxial compressive yield stresses ( $s_{bo}/s_{co}$ ), used in Eq. (2), may be chosen in between 1.10 and 1.16 (Lubliner et al. 1989). It is worth mentioning that 1.16 was respected in the current study because of the good agreement.

The dimensionless value of  $\beta$  can be estimated according to Eq. (3) by knowing the ratio of compressive-to-tensile effective cohesion stresses ( $s_c * \epsilon_{cc}^{pl}$ ) and ( $s_t * \epsilon_{tc}^{pl}$ ), respectively.

$$\beta * \epsilon^{pl} = \frac{s_c * \epsilon_c^{pl}}{s_t * \epsilon_{tc}^{pl}} * (1 - \alpha) + (1 + \alpha) \tag{3}$$

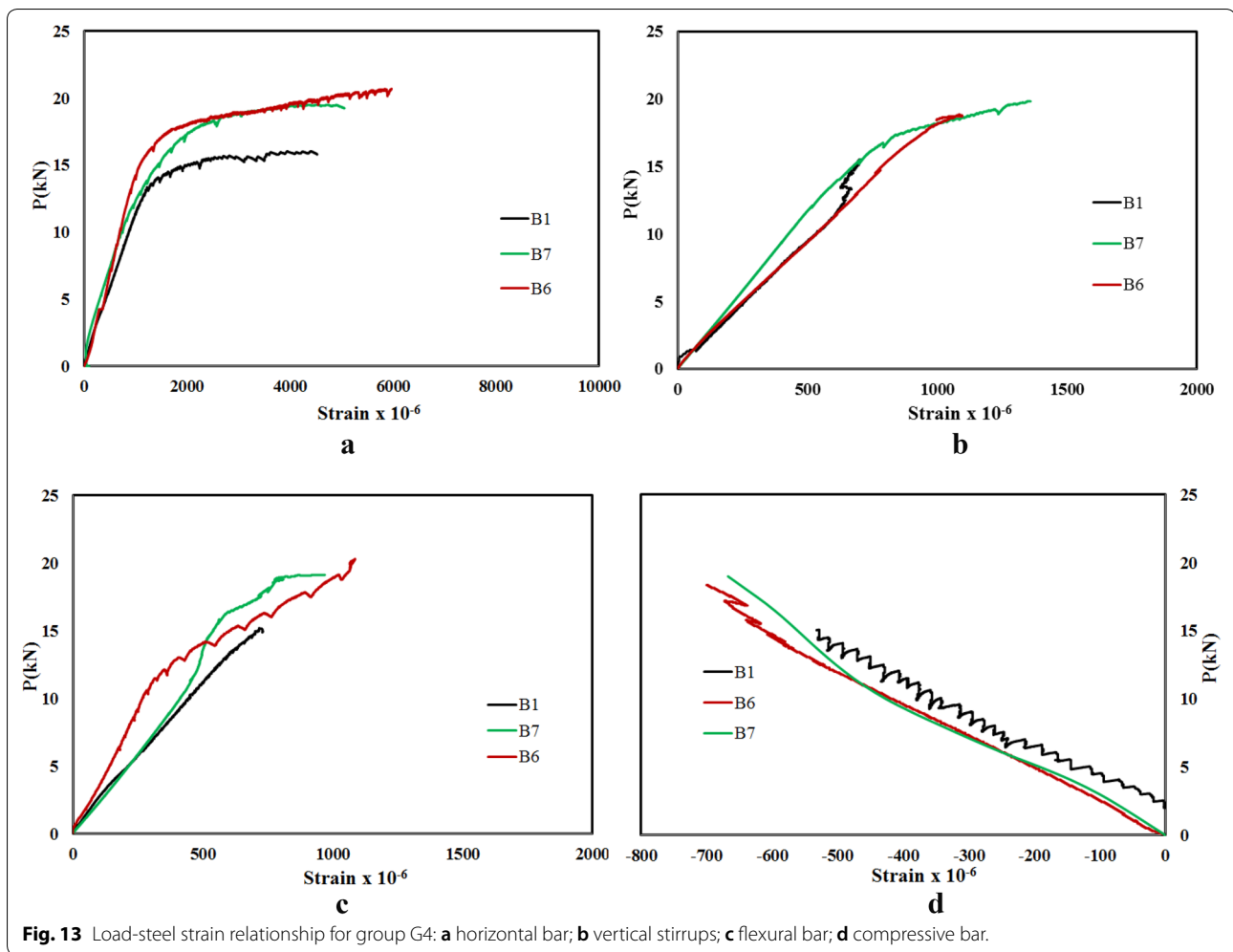
where  $\epsilon_{tc}^{pl}$  and  $\epsilon_{cc}^{pl}$  are the tensile and compressive effective cohesion plastic strains, respectively, while  $s_t$  and  $s_c$  are the tensile and compressive stresses, respectively.

By knowing the tensile-to-compressive meridian ratio namely in ABAQUS (ABAQUS/CAE 2014) program by ( $K$ ), the constant  $\gamma$  can be calculated in Eq. (4):

$$\gamma = \frac{3(1 - K)}{2 * K - 1} \tag{4}$$

The ratio of  $K$  can be selected in between 0.64 and 0.80 (Lubliner et al. 1989; Lee and Fenves 1998), while the default value of  $K=0.66$  (referred by ABAQUS program) showed an acceptable results.

The real stress–strain response for reinforcing steel bar tested experimentally can be shown in Fig. 3b. To constitute the FEA model with saved computational cost, the actual stress–strain relationship tested experimentally was idealized to piecewise linear curve representing an elastic zone followed by both hardening and softening behavior prior to failure as shown in Fig. 3b.



### 3.2 Model Set-up

A nonlinear three-dimensional FEA model was developed considering three main elements, namely: RC composite material, reinforced steel bars and rigid steel plates. The RC concrete beam was modelled as a solid continuum, while steel bars were modelled using wire elements. The model utilized the three-dimensional and eight-node linear hexahedral solid elements with reduced integration, namely: C3D8R to simulate concrete beam shape, in conjunction three-dimensional, two-node, truss elements, namely: T3D2 in ABAQUS software to simulate steel bars. Three thick steel plates with higher elastic stiffness were used in this modeling; one plate at the loading area and two plates at supports. Figure 15 shows view of the developed FEA model.

Perfect bond between reinforcing steel bars and the confined concrete was assumed to create the interaction between steel bars and surrounding concrete. This assumption was achieved using embedded element constraint available in ABAQUS software. In such constraint,

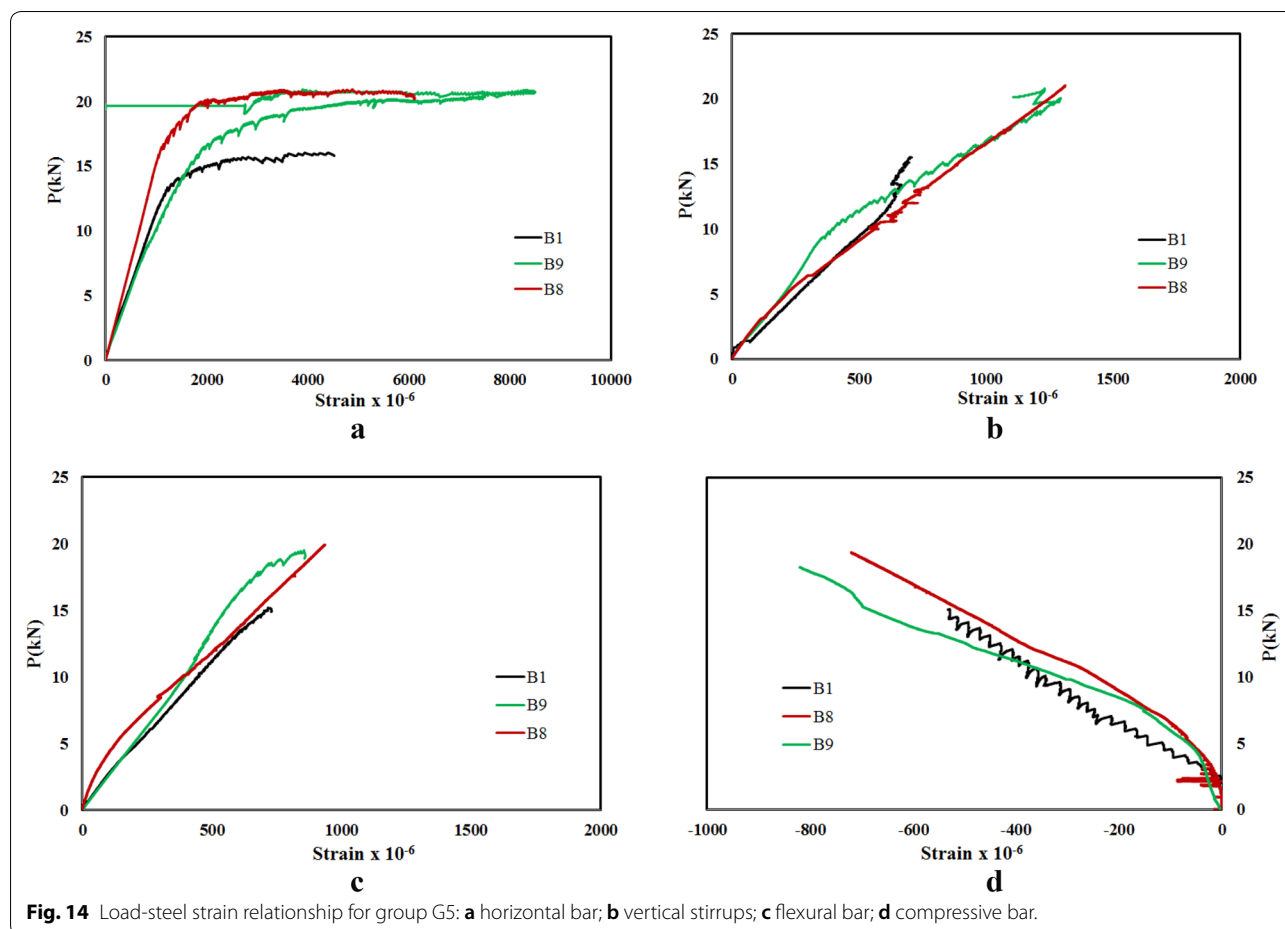
steel bars were selected to be embedded in the concrete beam as a host region.

### 3.3 Sensitivity of Numerical Parameters

Several attempts in the FE modelling were executed aiming to investigate the sensitivity and set-up the numerical parameters, namely: mesh density ( $l$ ) and dilation angle ( $\phi$ ). These numerical parameters were examined against the experimental findings for the two control models (B0 and B2) in terms of load–deflection response.

The FEA models were meshed with varying element sizes, namely: 10, 20, 25 and 50 mm, leading to dividing the beam width into 10, 5, 4 and 2 elements, respectively. The load–deflection response for control models obtained experimentally and using the FEA model can be seen in Fig. 16. It can be observed that mesh density with size of 10 and 20 mm presented a very close correlation with the experimental results prior to the ultimate stage with minor differences not exceeding about 2% in assessing the ultimate capacity. Due to the higher





computational cost that was observed for the FEA model with 10 mm mesh density, 20 mm mesh size was employed in model validation and assessment of the rest of the FEA models.

The dilation angle mainly used in the CDP modeling is to represent the vector direction of plastic strain increment as well as the increase of stress at shear-normal stress plane ( $p-q$ ) response. Since the shear region located beam the applied load location and the support in the modelled beam is subjected to biaxial or tri-axial confinement, the angle value can significantly affect the numerical analysis. The angle of dilation may be selected as 10°, 25° and 40° for thick flat slabs, shallow beams and corbels/deep beams, respectively (Bompa and Elghazouli 2017; Wosatko et al. 2015). The sensitivity study revealed that mesh density of 20 mm and dilation angle of 23° provided the best prediction of the structural response when compared to the experimental findings.

The other sensitive parameters used in the CDP model recommended elsewhere (Lubliner et al. 1989; Lee and Fenves 1998; Schickert and Winkler 1977) showed a satisfactory numerical results against those observed

experimentally with negligible differences and acceptable computational cost. Such sensitive parameters were defined as follows: ratio of the second stress invariant on the tensile meridian to that on the compressive meridian ( $k$ )=0.666, flow potential eccentricity ( $e$ )=0.1, the ratio of biaxial to uniaxial compressive yield stresses ( $f_{bo}/f_{co}$ )=1.16 and the time relaxation parameter (viscosity parameter)=0.00.

### 3.4 Model Validation

#### 3.4.1 Crack Pattern and Failure Mode

This section discusses and compares the results obtained experimentally and numerically from the static tests performed on the two control beams B0 and B2. Table 3 provides the recorded values of first visual cracking load  $P_{cr FE}$ , ultimate load  $P_u FE$ , maximum deflection at both cracking and ultimate stages;  $\Delta_{cr}$  and  $\Delta_u$  respectively. Figures 17 and 18 provide the tensile and compressive cracking visualization for the numerical models B0 and B2, respectively. It should be noted that cracking pattern view is available in ABAQUS software through maximum plastic strain. Cracking can be considered in CDP models

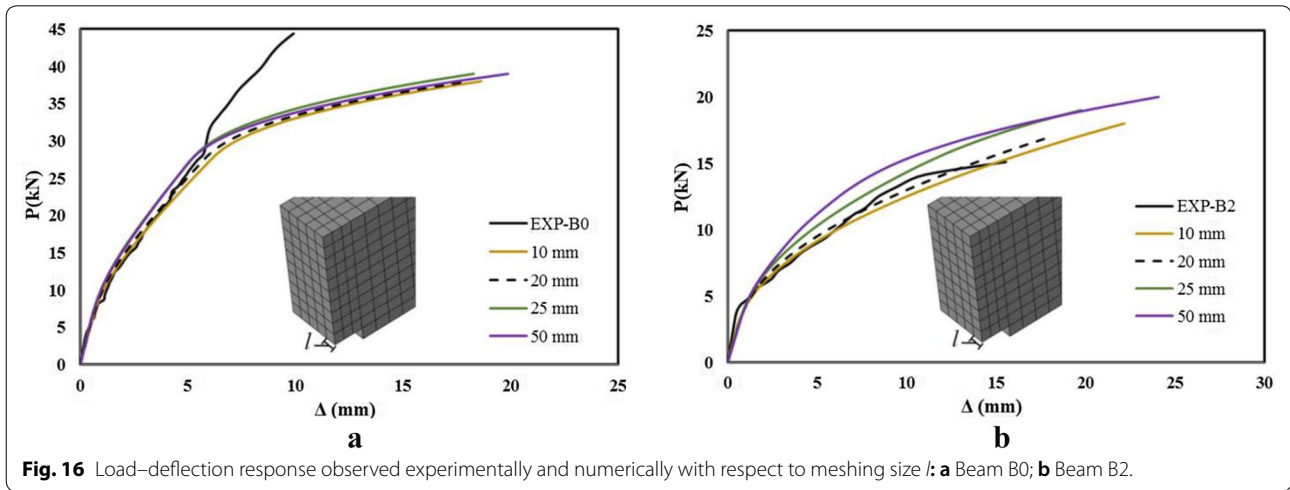
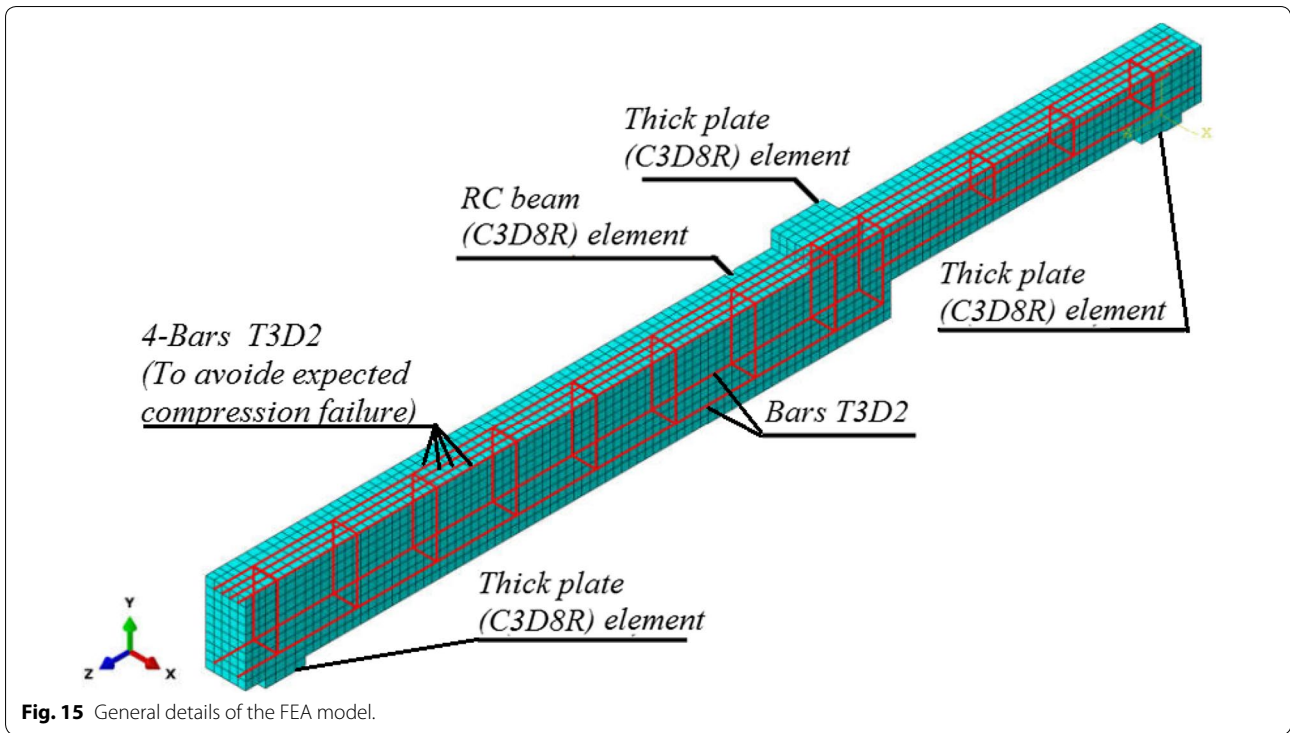
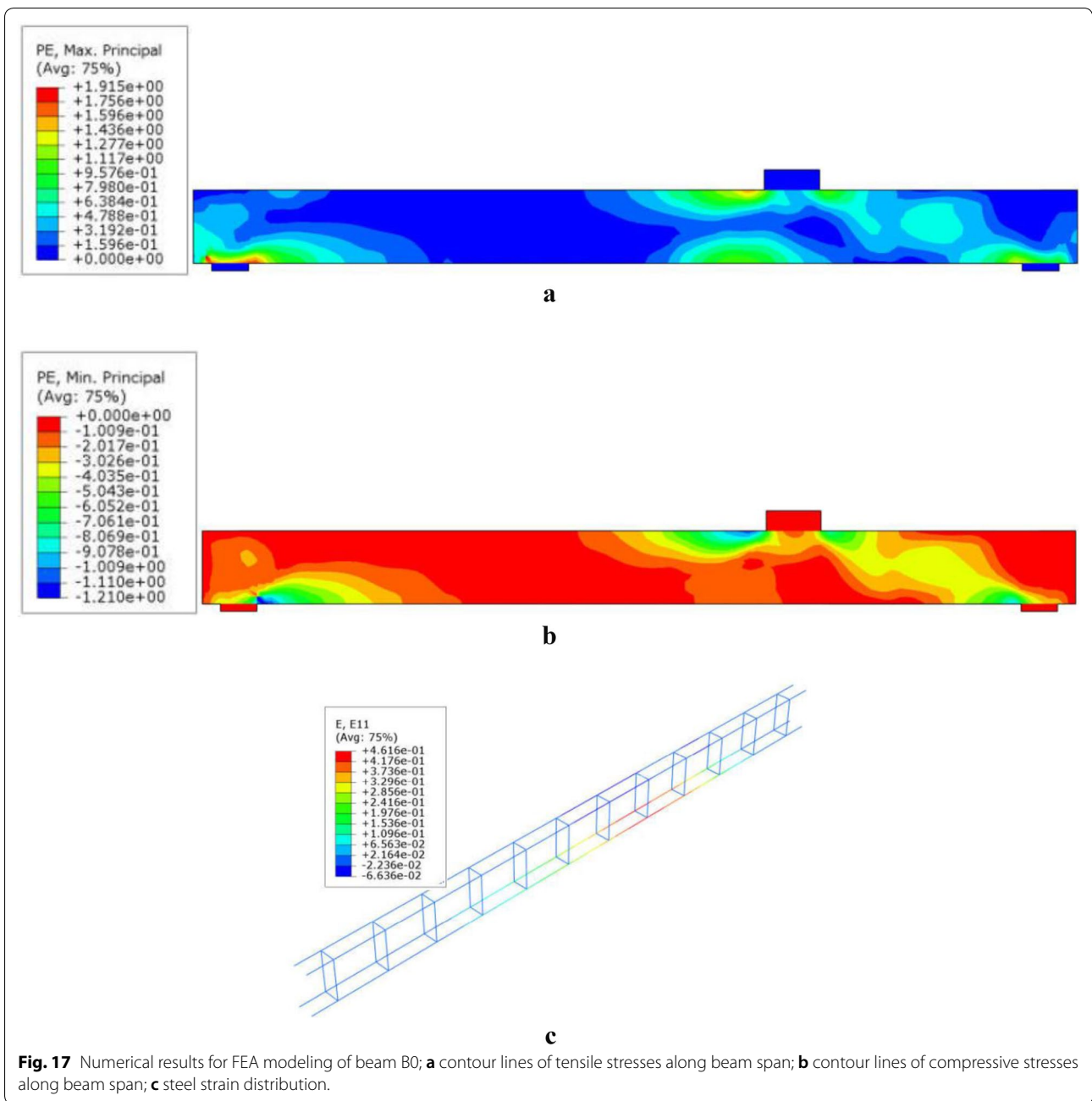


**Table 3 Comparison between FEA results and experimental findings for Group G1.**

Designation	Group	Cracking properties			$P_y$ (kN)	Location of first yield	$P_u$ (kN)	$\Delta_u$ (mm)	Mode of failure
		$P_{cr}$ (kN)	$\Delta_{cr}$ (mm)	Region					
EXP-B0	EXP. of G1	15.20	2.35	MS	33.8	F	44.40	9.91	SC
EXP-B2		3.00	0.45	RE	11.49	H	15.10	15.65	F
FEA-B0	FEA of G1	17.94	2.38	MS	31.00	F	40.40	14.75	SC
FEA-B2		3.81	1.88	RE	12.82	H	16.85	18.06	SC

$P_{cr}$ , load at which first crack occurred;  $\Delta_{cr}$ , deflection recorded at first crack;  $P_y$ , load at which first yield occurred;  $P_u$ , ultimate load;  $\Delta_u$ , deflection recorded at ultimate load; F, first yield load recorded at flexural bar; H, first yield load recorded at horizontal bar; MS, mid-length of strut connect between edge of loading plate and support; RE, re-entrant corner; SC, shear-compression failure; F, flexural failure.

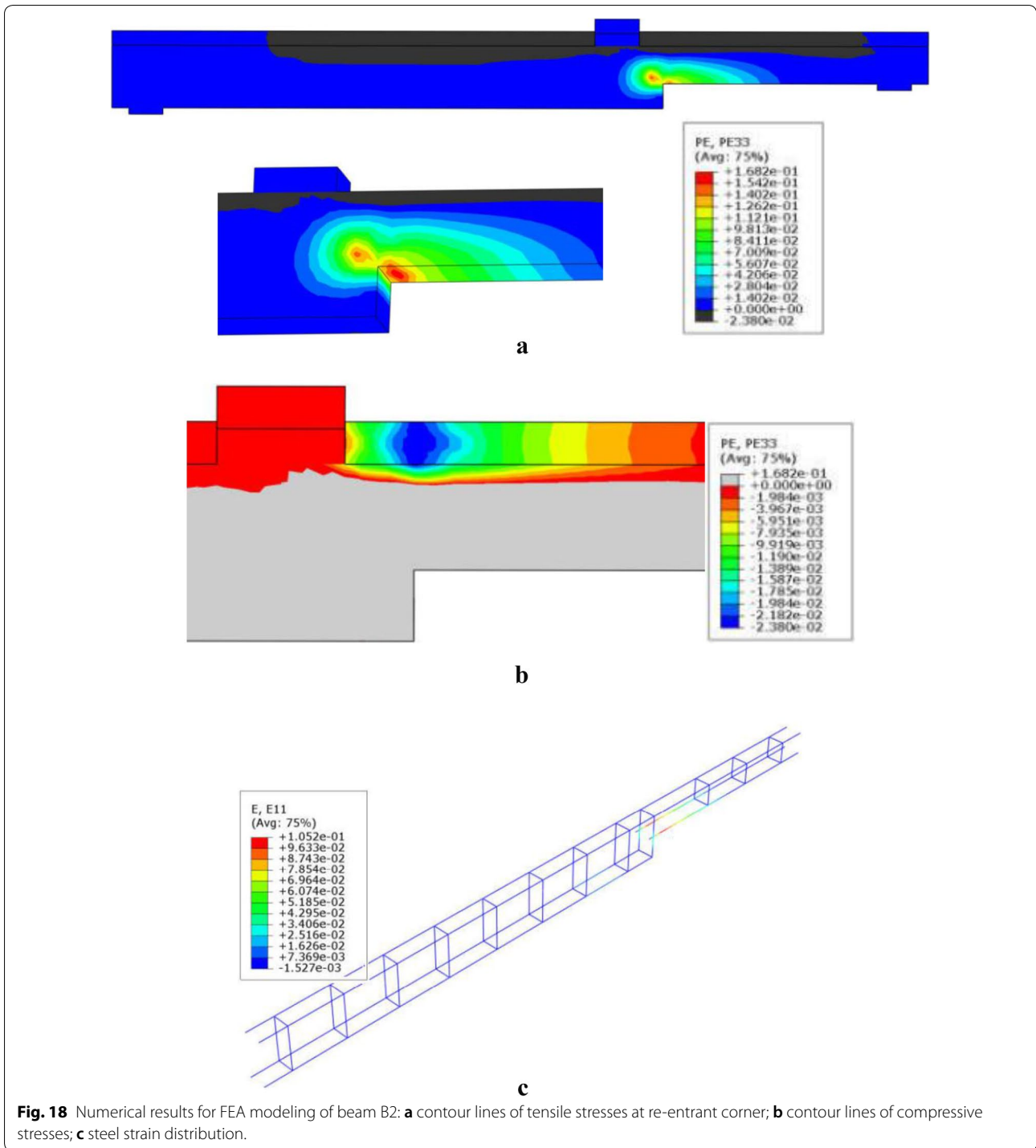


when maximum principle stresses achieve the positive sign. Also, the crack propagation is assumed to be perpendicular to maximum principle plastic strain.

Similar to experimental crack pattern of beam B0 shown in Fig. 5, numerical simulation shown in Fig. 17 shows tensile stresses causing the first cracking at the bottom beam-surface close to loading section at a load  $P_{cr FE}$  of 17.94 kN. Also, model B2 presented very critical stresses leading to first crack extending from re-entrant corner identical to that one observed experimentally as

shown in Figs. 5 and 18 for experimental and numerical modeling, respectively. Such cracking was predicted at a plastic tensile stress shown in Fig. 18a at a load  $P_{cr FE}$  of 3.81 kN.

At higher increments, significant compressive strut connecting between loading location and supporting plates for beam B0 was captured numerically as shown in Fig. 17b and experimentally in Fig. 5a. Significant tensile cracking stresses were observed initiating from re-entrant corner of beam B2 expanding upward towards



the loading plate zone as shown in the FEA model views in Fig. 18a and experimentally in Fig. 5b through appearance of flexural cracks.

Just before failure of beam B0, the major strut formed at shear zone grew presenting higher compressive stresses at its two ends (i.e. close to loading and

supporting plates) as shown in Fig. 17b. However, such compressive stresses were slightly excessive close to loading plate leading to failure at  $P_{uFE}$  of 40.40 kN (about 91% of  $P_{uEXP}$  as depicted in Table 3) with similar failure mode observed experimentally as shown in Fig. 5a. For FEA model B2, the major tensile cracking stresses formed at

re-entrant corner propagated upward towards top surface as shown in Fig. 18a, and then compressive stresses peaked at top surface in contact with the loading plate as shown in Fig. 18b, leading to failure at an ultimate load  $P_{u,FE}$  of 16.85 kN (about 11% greater than  $P_{u,EXP}$  as shown in Table 3). Such numerical compressive failure was almost similar to the brittle concrete crushing observed experimentally at the edge of loading plate shown in Fig. 5b reflecting the occurrence of compressive action.

**3.4.2 Load–deflection response**

Experimental and numerical load–deflection relationship measured at third-point of the beam span of the beams B0 and B2 are depicted in Fig. 19. Other than the earlier discussion regarding cracking load and mode of failure, one may observe that both numerical and experimental results showed similar elastic behavior ending at almost the same yield load with a difference of about 11% as shown in Table 3. Also, the load–deflection response for beam B2 shown in Fig. 19b shows good agreement between the FEA Modelling and the experimental findings.

**3.4.3 Load–Steel Strain Relationship**

Figures 20 and 21 show experimental and numerical load–steel strain response observed from gauges mounted on horizontal steel bar, vertical steel stirrup, flexural and compressive bars, respectively, for the two control beams B0 and B2. Table 3 compares the yield load values observed experimentally and numerically. Figures 17c and 18c present axial strain distributed along steel bars observed from FEA modelling for beams B0 and B2, respectively. Numerical results showed that the first observed yield load occurred in the flexural bar with

a value very close to that obtained experimentally for beam B0 (only with a difference about 9%) as shown in Table 3, while no yield was recorded in the flexural bar for beam B2 as shown in Fig. 21c. However, the FEA model of beam B2 showed that the horizontal bar had the identical essentiality experimental observation reflected, since it exhibited very similar yield load value recorded experimentally. In this context, it should be mentioned that FEA modelling results agreed with experimental outcome in terms of the yield location which occurred at the re-entrant corner, as expected. Also, numerical results indicated that negligible contribution was obtained from the vertical steel stirrups positioned in both sides of re-entrant corners. Therefore, it may be concluded that for beams with unequal depths, the sensitivity of the horizontal bar as shear reinforcement seemed to have a significant consideration compared to vertical closed stirrups. This may be attributed to the angle of crack propagation from re-entrant corner as shown in Figs. 18a and 5b for the numerical simulation and tested beam, respectively.

**4 Numerical Parametric Study**

Based on the verified FEA models, a parametric study was conducted to investigate the influence of various geometric variables on the structural response. These parameters are impact of T-section and width of D-region. FEA Results were compared in terms of cracking visualization, values of first cracking load and ultimate capacity, and the load–deflection response.

**4.1 Influence of T-Section**

This section examines the RC slab cast integrally with the beam with two unequal depths. Such T-shape beam was examined previously elsewhere (Kotsovou et al. 2016)

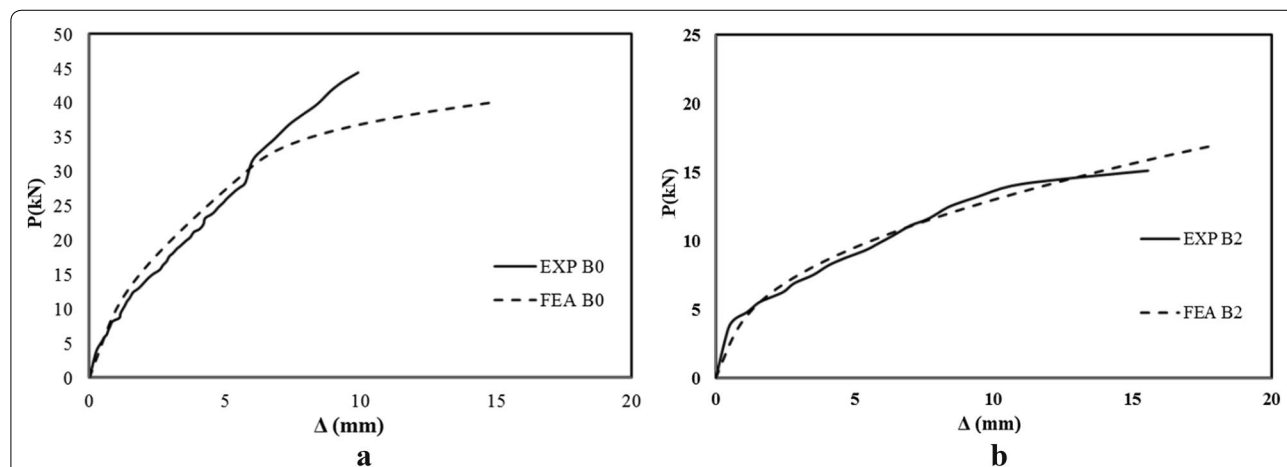
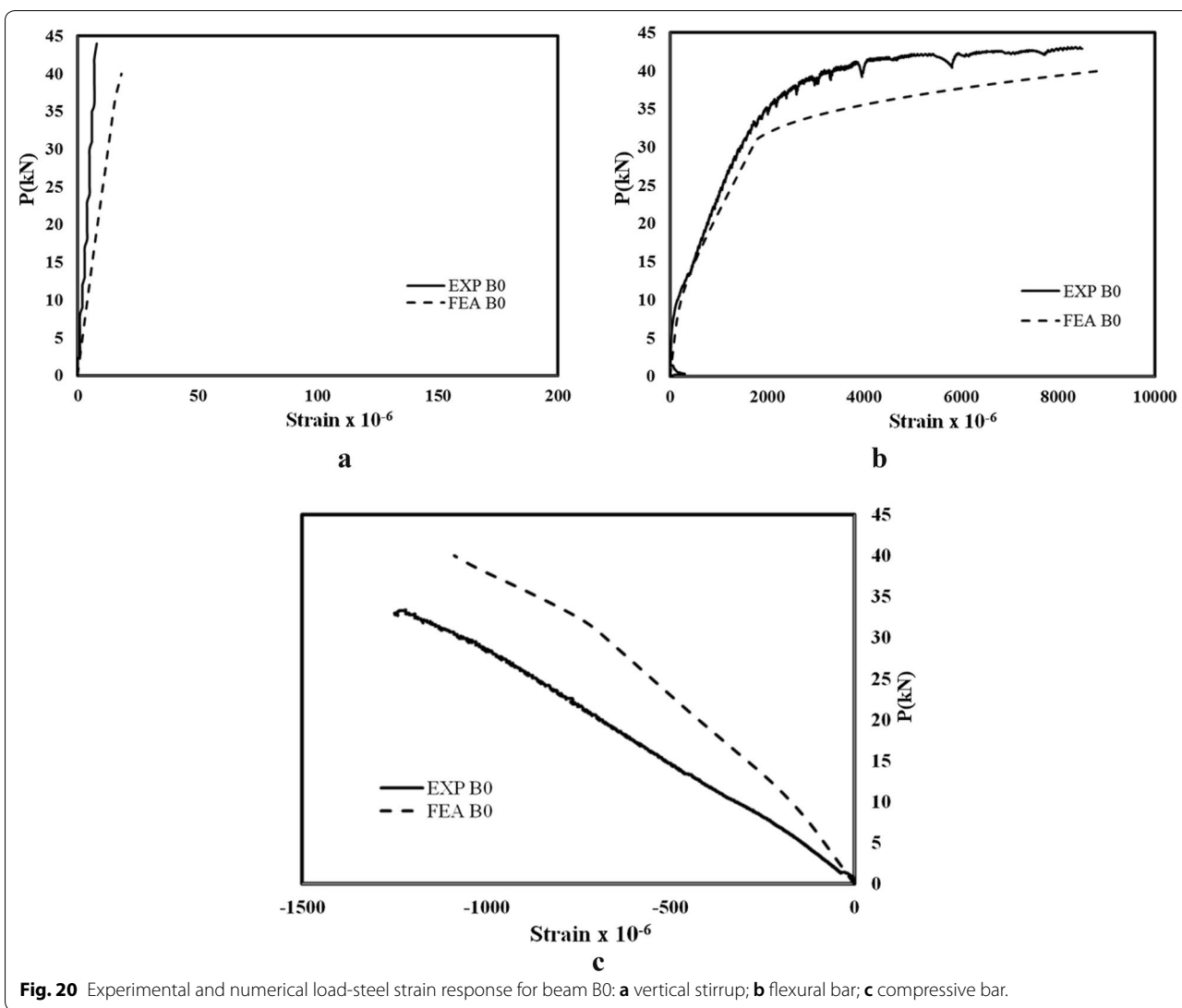


**Fig. 19** Load–deflection response observed experimentally and numerically: **a** load–deflection curve for beam B0; **b** load–deflection curve for beam B2.



when it is case with constant depth. Ciesielczyk et al. (2017) provided a numerical analysis to investigate material and geometric parameters mainly impact on T-section reinforced concrete beams. Results showed that slab thickness interacting with the beam has a significant influence on the ultimate capacity. However, the numerical models with thinner slab thickness may not provide a satisfactory contribution in beams with shear-compression failure mode. Deifalla and Ghobarah (2014) examined experimentally the behavior of inverted T-shaped RC beams subjected to combined shear and torsion stresses. The value of torsion-to-shear ratio significantly affects the performance of the inverted T-shaped beams in terms of cracking pattern; ultimate shear capacity and mode of failure. Also, it was found that the slab stirrups have significant effect in ultimate capacity.

To investigate the effect of the slab cast integrally with the beam of unequal depths on the overall behavior, two FEA models for beam B2 were developed examined with T-shaped section shown in Fig. 22a, b for the full-depth and partial depth portions of the beam. The slab thickness ( $t_f$ ) used in two models was 50 mm, while the slab width (B) was presented as the main variable per Kotsovou and Cotsovos (2018). In the first FEA model, the slab width shown in Fig. 22 was taken as  $B = 4t_f + b$  where b is the beam width, leading to slab width B of 300 mm. In the second FEA model, the slab width B was taken as 2d where d is the effective depth of beam, leading to B equal to 360 mm. The two FEA models were labeled as B-300 and B-360 for those having slab width of 300 and 360 mm, respectively, as shown in Table 4 and Fig. 22. It should be noted that other parameters in the two FEA

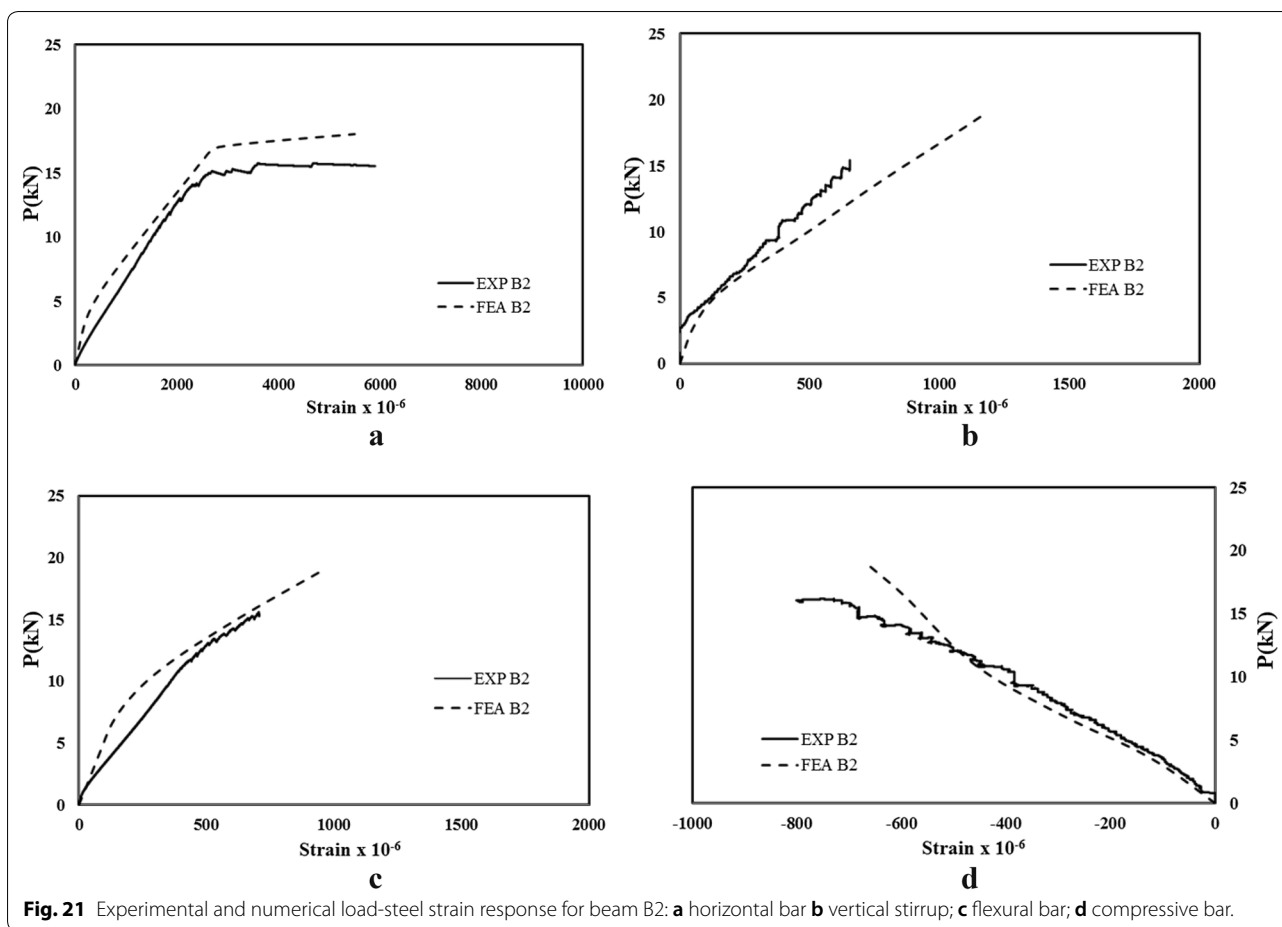


**Fig. 21** Experimental and numerical load-steel strain response for beam B2: **a** horizontal bar **b** vertical stirrup; **c** flexural bar; **d** compressive bar.

modelling were kept constant. Figure 22 shows geometrical details for the two FEA Models.

Test results shown in Fig. 22d shows significant increase in the load capacity of the beam with un-equal depths with the addition of the slab to resist applied load with the rectangular beam. Beam B-300 having a slab of width 300 mm exhibited a first cracking load 7 times greater than that for the same beam with rectangular cross-section. In case of the 360 mm slab, the first crack load was 7 times greater than that for a similar beam with rectangular section. Similar trend was observed in case of the yield load, showing an increase of 5 and 6 times that for a beam of rectangular section for B-300 and B-360 beams, respectively. Just before failure, it should be mentioned that the two FEA models yielded at approximately similar load values as shown in Table 4 which occurred at the horizontal bar positioned at the re-entrant corner as shown in Fig. 22e. The two FEA models failed due to excessive at the re-entrant corner followed compression failure in the slab. The contribution of the slab over the beam with unequal depth enhanced the ultimate capacity by 4 and 5 times that for a similar beam with rectangular

cross-section for B-300 and B-360 models, respectively, as shown in Table 4. Moreover, results showed that the slab-over-unequal depth beam can significantly affect the mode of failure from the sudden compressive mode (with lower ultimate capacity) to a ductile counterpart. Such ductile failure was observed by yielding the horizontal bar located at re-entrant corner followed by slab crushing at a higher load level.

#### 4.2 Influence D-Region Breadth

This section presents the influence of beam with depth having augmented width at the D-region as an attempt to enhance the ultimate capacity. György et al. (Nagy-György et al. 2012) carried out an experimental and numerical assessment on dapped-end RC beams with variables, namely: strengthening using sheets of fiber reinforced polymers, dapped-end height,  $h_n$ , recess,  $l_n$ , and cross-section web width,  $b$ . It was observed that both shear-to-span ratio as well as element geometric properties of cross-section can significantly affect yield load value recorded at steel bar reinforcing re-entrant corner. Conforti et al. (2015) performed an experimental study

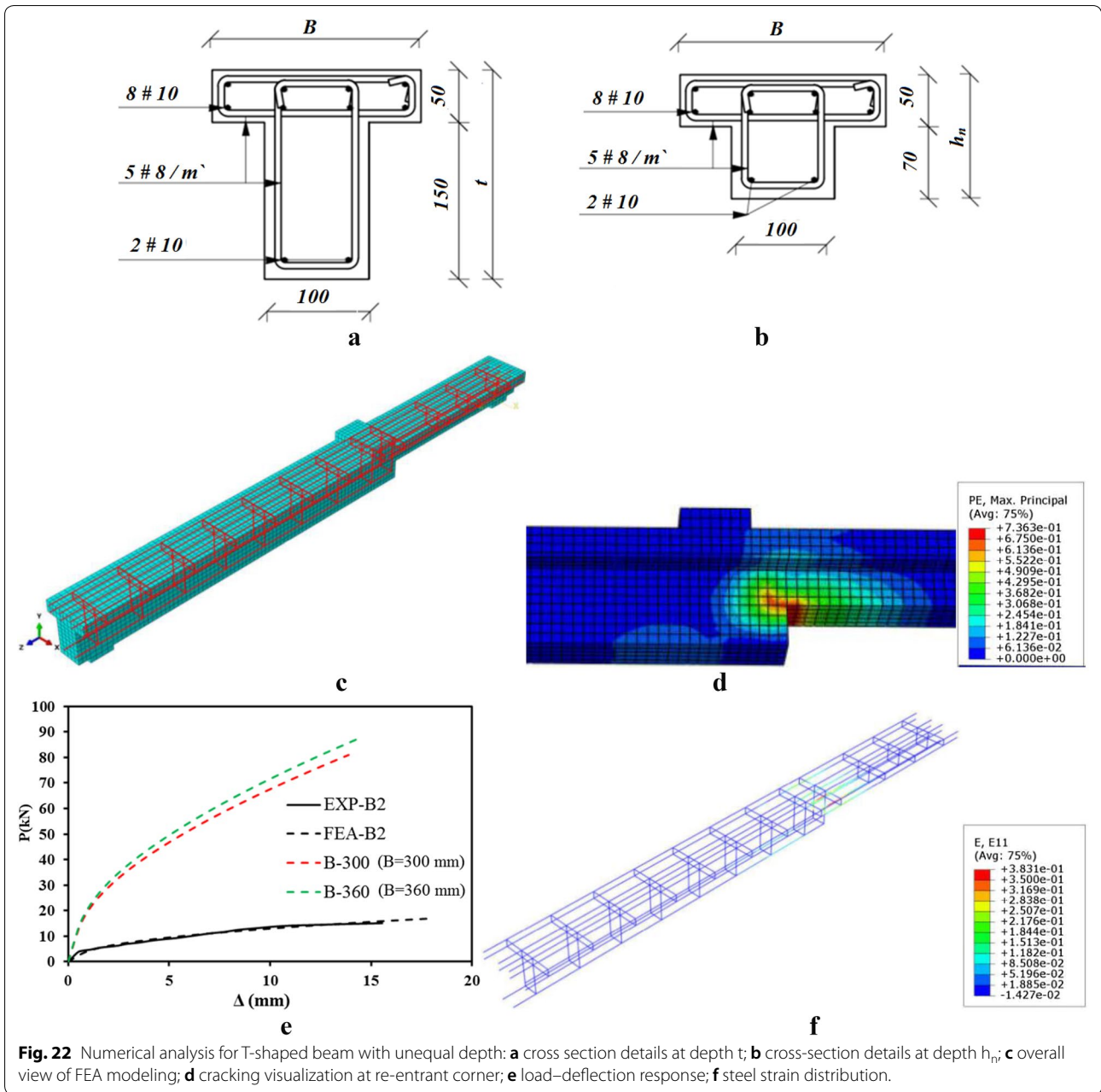


**Fig. 22** Numerical analysis for T-shaped beam with unequal depth: **a** cross section details at depth  $t$ ; **b** cross-section details at depth  $h_n$ ; **c** overall view of FEA modeling; **d** cracking visualization at re-entrant corner; **e** load–deflection response; **f** steel strain distribution.

**Table 4** FEA results of T-shaped cross sections.

FEM	B mm	t mm	$A_s$	Cracking properties				Yield properties			Ultimate properties			Failure mode
				$P_{cr}$ (kN)	$\Delta_{cr}$ (mm)	Position	$R_{cr}$	$P_y^*$ (kN)	$\Delta_y$ (mm)	$R_y$	$P_u$ (kN)	$\Delta_u$ (mm)	$R_u$	
FEA-B2	–	–	–	3.81	1.88	RE	–	12.82	10.02	–	16.85	18.06	–	Shear-failure
B-300	300	50	8#10	27.34	1.70	RE	7	69.00	10.38	5	81.00	13.78	4.50	
B-360	360	50	–	32.57	2.11	RE	8	74.19	10.62	6	88.00	14.55	4.88	

RE, re-entrant corner;  $P_y^*$  The all values of yield load were recorded at horizontal bar positioned at re-entrant corner; B and t, width and thickness of slab interacting over beam, respectively;  $A_s$ , steel reinforcement used in slab;  $P_{cr}$ , load at which first crack occurred;  $\Delta_{cr}$ , deflection recorded at first cracking;  $R_{cr}$ , ratio between cracking load occurred at each model over that of B2;  $P_y$ , load at which first yield occurred;  $\Delta_y$ , deflection recorded at yield load;  $R_y$ , ratio between yield load occurred at each model over that of B2;  $P_u$ , ultimate load;  $\Delta_u$ , deflection recorded at ultimate load;  $R_u$ , ratio between ultimate load occurred at each model over that of B2.



on RC wide-shallow beams subjected to a shear force, focusing on the role of the width-to-effective depth ratio ( $b/d$ ) and on the beneficial influence of newly developed polypropylene fibers. Results indicated that beams having width-to-effective depth ratio from 2 to 3 presented a very higher ultimate shear stress compared to the other rivals by about 30–40%.

In order to gain a better insight into the impact of width on the current unequal depth beam, three FEA models were numerically executed. Two FEA models were created with the identical overall geometric and material properties defined earlier for beam B2 except the width of D-region changed to 150 mm and 200 mm (namely B-150 and B-200 respectively as listed in Table 5). The increased width was set along sufficient specified length of D-region ( $l_d$ ) as shown in Fig. 23a where the tensile stresses reached its peak. Such  $l_d$  length was taken as 400 mm. The third FE model B-150-2100 had the same increase width of 150 mm but over the entire length of beam of 2100 mm. The third FEA model was aimed at presenting the major variance compared to the second counterpart B-150. Table 5 presents the geometric details of the three FEA models along with the original FEA model for beam B2.

Table 5 showed that first cracking stage has been affected by the beam breadth at D-region, since both FEA models B-150 and B-200 presented higher cracking load than that of FEA model for beam B2 (see column 7 in Table 5). The first cracking appearance was also detected diagonally extending from re-entrant corner. It should be noted that comparison between B-150 and B-150-2100 resulted in approximately similar first cracking load which was about 2.8 times  $P_{cr}$  obtained from the FEA model for beams BS. Table 5 shows the first yield load, which was recorded by horizontal bar at point located close to re-entrant corner, was greater than that obtained for beam B2 by about 82%, 117% and 68% for models B-150, B-200 and B-150-2100, respectively. It should be mentioned that yield stage was observed at a level just prior to the ultimate load which was about 92%, 96%

and 83% of  $P_u$  for models B-150, B-200 and B-150-2100, respectively. Beyond yield, the executed FEA models lost the ability to sustain any applied load leading to failure at the re-entrant corner due to excessive stresses as shown Fig. 23b. The ultimate load was augmented above that for beams B2 by about 48%, 72% and 54% for models B-150, B-200 and B-150-2100, respectively.

Comparison between B-150 and B-150-2100 model resulted in almost very similar enhancement compared to the control beam B2. So, improving cracking, yield and ultimate performance of unequal depth beams by increasing the breadth of D-region was found to be a better candidate compared to increasing the beam width long the whole span length, especially when the minimum cost is the main requirement in design.

## 5 Conclusion

This paper investigates the behavior of RC beam with unequal depths in the form of cracking load, yield load, ultimate carrying capacity and crack pattern. Depth and length of the beam nib were the geometrical variables, while variation in shear reinforcement was considered through an additional steel ratio and layout. Ten RC beams were experimentally tested up to failure. A nonlinear three-dimensional FEA analysis was created on two RC beams and validated using the experimental findings. The following conclusions can be drawn from this study:

- The location of re-entrant corner affects cracking characteristics, yield load, and ultimate load capacity. Experimental results showed that increasing the beam nib height-to-recess length ratio from 0.19 to 0.23 and 0.38 increases the yield load by 27% and 94% and ultimate load by 4% and 64%, respectively. In addition, the mode of failure changes from pure flexural to compression-shear failure with the decrease in nib length.
- Experimental results showed significant enhancement in the beam ultimate load carrying capacity when using additional closed stirrups along the

**Table 5** FEA results of RC beams with enlarged width over portion of the beam.

FEM	b mm	$l_d$ mm	$A_s$	Cracking properties			Yield properties			Ultimate properties			Failure mode
				$P_{cr}$ (kN)	$\Delta_{cr}$ (mm)	$R_{cr}$	$P_y^{**}$ (kN)	$\Delta_y$ (mm)	$R_y$	$P_u$ (kN)	$\Delta_u$ (mm)	$R_u$	
FEA-B2	–	–	8#10	3.81	1.88	–	12.82	10.02	–	16.85	18.06	–	Shear-failure
B-150	150	400		10.67	3.42	2.80	23.30	24.63	1.82	25	31.25	1.48	
B-200	200	400		14.67	5.43	3.85	27.86	26.94	2.17	29	34.14	1.72	
B-150-2100	150	2100		10.59	2.82	2.77	21.56	15.31	1.68	26	30.61	1.54	

$l_d$ , length of D-region at where width of beam cross-section increased;  $P_{cr}$ , load at which first crack occurred;  $\Delta_{cr}$ , deflection recorded at first cracking;  $R_{cr}$ , ratio between cracking load occurred at each model over that of B2;  $P_y$ , load at which first yield occurred;  $\Delta_y$ , deflection recorded at yield load;  $R_y$ , ratio between yield load occurred at each model over that of B2;  $P_u$ , ultimate load;  $\Delta_u$ , deflection recorded at ultimate load;  $R_u$ , ratio between ultimate load occurred at each model over that of B2.

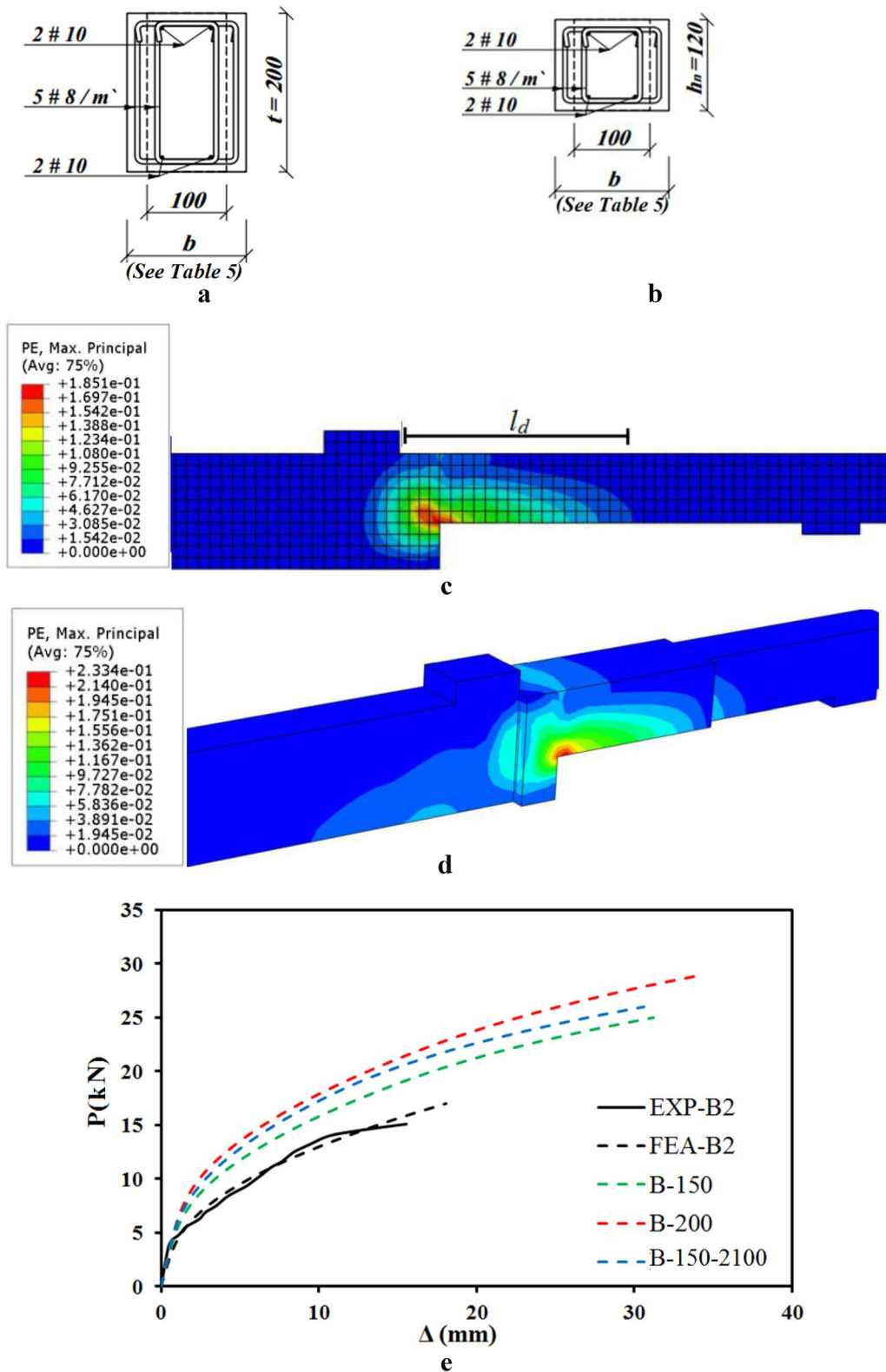


**Fig. 23** Numerical analysis of RC unequal depth beam with variable width: **a** cross section details at depth  $t$ ; **b** cross-section details at depth  $h_n$ ; **c** contour lines of tensile stresses from FEA model of beam B2 showing  $l_d$  with shear concentration; **d** contour lines of tensile stresses in beam B2 with enlarged width over  $l_d$  and the right side of the applied load location; **e** load-deflection response.

entire beam span excluding/including nib zone. On the other hand, adding closed stirrups at only the nib zone seemed to have negligible contribution to the load-carrying capacity.

- The use of bent-up bars with ratio of 0.52% at the re-entrant corner resulted in better deflection response and lower damage at re-entrant corner compared to the findings due to the increase in the shear reinforcement ratio along the entire span.
- Good agreement between experimental and FEA results proved the efficiency of the developed numerical model in capturing the nonlinear behavior of the RC beam with unequal depths as depicted from load–deflection response, cracking, failure modes and strain development in reinforcement. Hence, the developed three-dimensional FEA model can be used as a tool for further studies in future.
- Numerical and experimental results confirmed that for RC beams with unequal depths, the sensitivity of the horizontal bar as shear reinforcement seemed to have a significant effect compared to vertical closed stirrups at the re-entrant corner. This may be attributed to the angle of crack growing from re-entrant corner. Also, the position of re-entrant corner can significantly affect the yield load since a higher yield load was reached when using smaller recess length.
- Numerical and experimental findings showed that critical stresses have been generated from re-entrant corner at the initiation of first shear cracking. Also, numerical results agreed with experimental observation in terms of yield location which occurred at the re-entrant corner due to excessive tensile stresses.
- The presence of RC slab, that is cast integrally over the beam with unequal depth, has significant contribution to crack patterns and characteristics (by about 7 to 8 times higher than the non-slab one) as well as yield load values (by about 5 to 6 times higher than the non-slab one) based on the size of the beams considered in this research. Moreover, the presence of the slab changed the mode of failure from the sudden compressive mode (with lower ultimate capacity) to the ductile counterpart (with higher ultimate load).
- Numerical results showed that increasing breadth at D-region (where re-entrant corner exists) by about 50% to 100% resulted in an increase in initial cracking and yield load. Also, the ultimate load capacity has been augmented by about 48% to 72% based on the studies widths in this research. The increase in beam width in only the D-region was found to be more economical and gives better results compared to increasing beam breadth along the whole span length.
- Given the proper development length of the nib tension reinforcement at the re-entrant zone, bond/anchorage failure of such bars was precluded in this study. Design engineer should be attention to bar anchorage length in practice to promote global failure of the beam.

#### Acknowledgements

The authors acknowledge the contributions of technical staff at Kafrelsheikh University, Egypt, for providing great assistance and helpful comments in executing the experimental program.

#### Authors' contributions

All authors contributed to the paper. All authors read and approved the final manuscript.

#### Availability of data and materials

The experimental data can be obtained through email communication with the first author at ahmed\_hamoda@eng.kfs.edu.eg.

#### Competing interests

The authors declare that they have no competing interests.

#### Author details

<sup>1</sup> Civil Engineering Dept, Faculty of Engineering, Kafrelsheikh University, Kafrelsheikh, Egypt. <sup>2</sup> Civil Engineering Department, Ryerson University, Toronto, ON, Canada.

Received: 22 April 2019 Accepted: 28 August 2019

Published online: 18 November 2019

#### References

- ABAQUS/CAE (2014) Finite Element Analysis program version 6.14-3.
- Alam, M. A., Sami, A., & Mustapha, K. N. (2017). Embedded connectors to eliminate debonding of steel plate for optimal shear strengthening of RC beam. *Arabian Journal for Science and Engineering*, 42(9), 4053–4068.
- Aswin M, Mohammed BS, Liew MS, Syed ZI. Shear failure of RC dapped-end beams. *Advances in Materials science and engineering*. 2015; 2015.
- Bompa, D. V., & Elghazouli, A. Y. (2017). Numerical modelling and parametric assessment of hybrid flat slabs with steel shear heads. *Engineering Structures*, 1(142), 67–83.
- Carreira, D. J., & Chu, K. H. (1985). Stress–strain relationship for plain concrete in compression. *ACI Journal*, 82(6), 797–804.
- Chiu, C. K., Ueda, T., Chi, K. N., & Chen, S. Q. (2016). Shear crack control for high strength reinforced concrete beams considering the effect of shear-span to depth ratio of member. *International Journal of Concrete Structures and Materials*, 10(4), 407–424.
- Choi, W. C., Jang, S. J., Kim, S. H., & Yun, H. D. (2018). Shear performance of embedded anchor plates in reinforced concrete tilt-up panels under monotonic and cyclic loadings. *Archives of Civil and Mechanical Engineering*, 18(2), 430–441.
- Ciesielczyk, K., Szumigala, M., & Ścigała, J. (2017). The numerical analysis of the effective flange width in T-section reinforced concrete beams. *Procedia Engineering*, 1(172), 178–185.
- Conforti, A., Minelli, F., Tinini, A., & Plizzari, G. A. (2015). Influence of polypropylene fibre reinforcement and width-to-effective depth ratio in wide-shallow beams. *Engineering Structures*, 1(88), 12–21.
- Deifalla, A., & Ghobarah, A. (2014). Behavior and analysis of inverted T-shaped RC beams under shear and torsion. *Engineering Structures*, 1(68), 57–70.
- Demir, A., Caglar, N., Ozturk, H., & Sumer, Y. (2016). Nonlinear finite element study on the improvement of shear capacity in reinforced concrete T-Section beams by an alternative diagonal shear reinforcement. *Engineering Structures*, 1(120), 158–165.

- Desnerck, P., Lees, J. M., & Morley, C. T. (2016). Impact of the reinforcement layout on the load capacity of reinforced concrete half-joints. *Engineering Structures*, 15(127), 227–239.
- Desnerck, P., Lees, J. M., & Morley, C. T. (2017). The effect of local reinforcing bar reductions and anchorage zone cracking on the load capacity of RC half-joints. *Engineering Structures*, 1(152), 865–877.
- Desnerck, P., Lees, J. M., & Morley, C. T. (2018). Strut-and-tie models for deteriorated reinforced concrete half-joints. *Engineering Structures*, 15(161), 41–54.
- El Bitouri, Y., Jamin, F., Pélioussou, C., & El Youssoufi, M. S. (2017). Tensile and shear bond strength between cement paste and aggregate subjected to high temperature. *Materials and Structures*, 50(6), 234.
- Fang, Z., Jiang, H., Liu, A., Feng, J., & Chen, Y. (2018). Horizontal Shear Behaviors of Normal Weight and Lightweight Concrete Composite T-Beams. *International Journal of Concrete Structures and Materials*, 12(1), 55.
- Fernández-Ruiz, M. A., Gil-Martín, L. M., & Hernández-Montes, E. (2018). Structural performance of RC beams containing tension-only nodes. *International Journal of Concrete Structures and Materials*, 12(1), 7.
- Hamoda, A., Hossain, K. M., Sennah, K., Shoukry, M., & Mahmoud, Z. (2017). Behaviour of composite high performance concrete slab on steel I-beams subjected to static hogging moment. *Engineering Structures*, 1(140), 51–65.
- Hawileh, R. A., Abdalla, J. A., Fardmanesh, F., Shahsana, P., & Khalili, A. (2017). Performance of reinforced concrete beams cast with different percentages of GGBS replacement to cement. *Archives of Civil and Mechanical Engineering*, 17(3), 511–519.
- Hossain, K. M. A., Hamoda, A. A., Sennah, K., Shoukry, M. E., & Mahmoud, Z. I. (2015). Bond strength of ribbed GFRP bars embedded in high performance fiber reinforced concrete. *Journal of Multidisciplinary Engineering Science and Technology*, 2(6), 1260–1267.
- Hu, B., & Wu, Y. F. (2018). Effect of shear span-to-depth ratio on shear strength components of RC beams. *Engineering Structures*, 1(168), 770–783.
- Kassem, W. (2015). Strength prediction of corbels using strut-and-tie model analysis. *International Journal of Concrete Structures and Materials*, 9(2), 255.
- Kobiela, S., & Zamiar, Z. (2017). Oval concrete domes. *Archives of Civil and Mechanical Engineering*, 17(3), 486–501.
- Kotsovou, G. M., & Cotsovos, D. M. (2018). Shear failure criterion for RC T-beams. *Engineering Structures*, 1(160), 44–55.
- Kotsovou, G. M., Cotsovos, D. M., Tanjung, J., Aryanti, R., Nur, O. F., & Devinus, A. (2016). Shear strength of reinforced concrete T-beams without stirrups. *J Eng Sci Technol*, 11(4), 548–562.
- Lee, J., & Fenves, G. L. (1998). Plastic-damage model for cyclic loading of concrete structures. *Journal of engineering mechanics, ASCE*, 124(8), 892–900.
- Lim, K. M., Shin, H. O., Kim, D. J., Yoon, Y. S., & Lee, J. H. (2016). Numerical assessment of reinforcing details in beam-column joints on blast resistance. *International Journal of Concrete Structures and Materials*, 10(3), 87–96.
- Lublinter, J., Oliver, J., Oller, S., & Oñate, E. (1989). A plastic-damage model for concrete. *International Journal of Solids and Structures*, 25, 299–326.
- Nagrodzka-Godycka, K., & Piotrkowski, P. (2012). Experimental Study of Dapped-End Beams Subjected to Inclined Load. *ACI Structural Journal*, 109, 1.
- Nagy-György, T., Sas, G., Dăescu, A. C., Barros, J. A., & Stoian, V. (2012). Experimental and numerical assessment of the effectiveness of FRP-based strengthening configurations for dapped-end RC beams. *Engineering Structures*, 1(44), 291–303.
- Naik, U., & Kute, S. (2013). Span-to-depth ratio effect on shear strength of steel fiber-reinforced high-strength concrete deep beams using ANN model. *International Journal of Advanced Structural Engineering*, 5(1), 29.
- Nosheen, H., Qureshi, L. A., Tahir, M. F., & Rashid, M. U. (2018). An investigation on shear behavior of prestressed concrete beams cast by fiber reinforced concrete. *Arabian Journal for Science and Engineering*, 1, 1–9.
- Pradhan, S., Kumar, S., & Barai, S. V. (2018). Performance of reinforced recycled aggregate concrete beams in flexure: experimental and critical comparative analysis. *Materials and Structures*, 51(3), 58.
- Qeshta, I. M., Shafiqh, P., & Jumaat, M. Z. (2016). Research progress on the flexural behaviour of externally bonded RC beams. *Archives of Civil and Mechanical Engineering*, 16(4), 982–1003.
- Sas, G., Dăescu, C., Popescu, C., & Nagy-György, T. (2014). Numerical optimization of strengthening disturbed regions of dapped-end beams using NSM and EBR CFRP. *Composites Part B Engineering*, 1(67), 381–390.
- Schickert G, Winkler H. Results of test concerning strength and strain of concrete subjected to multi-axial compressive stress. Ger. Comm, reinforced concrete, 1977, Heft 277, Berlin.
- Wosatko, A., Pamin, J., & Polak, M. A. (2015). Application of damage-plasticity models in finite element analysis of punching shear. *Computers & Structures*, 15(151), 73–85.
- Zhong, J. T., Wang, L., Deng, P., & Zhou, M. (2017a). A new evaluation procedure for the strut-and-tie models of the disturbed regions of reinforced concrete structures. *Engineering Structures*, 1(148), 660–672.
- Zhong, J. T., Wang, L., Deng, P., & Zhou, M. (2017b). A new evaluation procedure for the strut-and-tie models of the disturbed regions of reinforced concrete structures. *Engineering Structures*, 1(148), 660–672.

## Publisher's Note

Springer Nature remains neutral with regard to jurisdictional claims in published maps and institutional affiliations.

Submit your manuscript to a SpringerOpen® journal and benefit from:

- Convenient online submission
- Rigorous peer review
- Open access: articles freely available online
- High visibility within the field
- Retaining the copyright to your article

Submit your next manuscript at ► [springeropen.com](https://www.springeropen.com)